Computational Fluid Dynamics (CFD) Simulation of Microfluidic Focusing in a Low-Cost Flow Cytometer

by
Connor Parrott

A THESIS

submitted to

Oregon State University

Honors College

in partial fulfillment of
the requirements for the
degree of

Honors Baccalaureate of Science in Mechanical Engineering
(Honors Scholar)

Presented June 2, 2017
Commencement June 2017

AN ABSTRACT OF THE THESIS OF

Connor Parrott for the degree of Honors Baccalaureate of Science in Mechanical Engineering presented on June 2, 2017. Title: Computational Fluid Dynamics (CFD) Simulation of Microfluidic Focusing in a Low-Cost Flow Cytometer.

Abstract approved:_____

Nordica MacCarty

Inertial microfluidics refers to the manipulation of the location and velocity of particles suspended in microscale fluid flow without the introduction of outside forces. It has promising applications in flow cytometry and other biomedical technologies because of the potential for lowering cost and complexity relative to current particle focusing methods. Utilizing inertial microfluidics requires accurately modeling the effects of inertial forces acting on particles. This paper explores a method of predicting the trajectory of microscale particles using the Discrete Phase Model of the ANSYS Fluent CFD software. A model was developed for the effects of inertial lift on solid particles in Poiseuille flow. This method was observed to have good agreement with empirical results when modeling the behavior of neutrally buoyant spherical particles experiencing non-negligible laminar flow in straight circular channels. The particles were observed to focus to an equilibrium annulus of about 0.6 the diameter of the channel. The speed with which they focused was observed to vary proportionally with particle diameter and Reynolds number, corresponding with empirical results.

Key Words: CFD, flow cytometry, microfluidics, inertial focusing, fluid dynamics

Corresponding e-mail address: parrottc@oregonstate.edu

Computational Fluid Dynamics (CFD) Simulation of Microfluidic Focusing in a Low-Cost Flow Cytometer

by
Connor Parrott

A THESIS

submitted to

Oregon State University

Honors College

in partial fulfillment of
the requirements for the
degree of

Honors Baccalaureate of Science in Mechanical Engineering
(Honors Scholar)

Presented June 2, 2017
Commencement June 2017

Honors Baccalaureate of Science in Mechanical Engineering project of Connor Parrott presented on June 2, 2017.

APPROVED:

_____

Nordica MacCarty Mentor, representing Mechanical Engineering

_____

Deborah Pence Committee Member, representing Mechanical Engineering

_____

Wesley Smith Committee Member, representing Thermo Fisher Scientific

_____

Toni Doolen, Dean, Oregon State University Honors College

I understand that my project will become part of the permanent collection of Oregon State University, Honors College. My signature below authorizes release of my project to any reader upon request.

_____

Connor Parrott, Author

Acknowledgments

I would like to thank Wesley Smith for bringing my attention to flow cytometry and being a very proactive and helpful sponsor during the senior project that inspired this thesis. I would like to thank Dr. Deborah Pence for her guidance and advice as well as inspiring my interest in fluid mechanics and computational fluid dynamics. I would also like to thank both of the aforementioned two for being willing to serve on my thesis committee. I would like to thank the two other members of my senior project design team, Davis Raye and Tyler Vonderach. I would like to thank my parents and family for supporting me and encouraging me during this process. Finally, I would like to thank Dr. Nordica MacCarty for being such a helpful and inspiring mentor. It was her encouragement that motivated me to overcome the obstacles that I thought were in my way and complete this thesis.

Table of contents

1 Introduction

This paper details the efforts to develop a method for simulating the motion of particles under the effects of inertial lift in microscale flow. This has applications in multiple biomedical fields, especially flow cytometry. Flow cytometry is a medical technology for analyzing the size, shape, and other characteristics of cells and other microscopic particles. It works by suspending the particles in a stream of fluid and passing the stream through an electronic detection apparatus, usually a laser or an electric impedance device. It has many uses in medicine and biology, including cell counting, cell identification, and cell sorting. As the cells pass through the detection beam, the way they cause the beam to bend, deflect, or otherwise change is detected by a sensor array. These changes to the beam are interpreted by accompanying software in order to determine cell characteristics.

Thermo Fisher Scientific is a biotechnology company based in Waltham, Massachusetts [1]. One of their primary product lines is flow cytometers. The science of flow cytometry is discussed in greater detail in Section 2. Thermo Fisher Scientific approached the Oregon State University School of Mechanical, Industrial and Manufacturing Engineering (MIME) with the proposal of a low-cost flow cytometer project for the MIME Capstone Design class. This project would entail the design and construction of a prototype flow cytometer as a proof-of-concept. Most flow cytometer models currently on the market are complicated and expensive to build and operate, and the design of a simpler and less costly model would greatly expand the size of the potential customer base [2].

In coordination with the project sponsor at Thermo Fisher Scientific, the Capstone cytometer design team drew up a list of project requirements and the subsystems that would be required to implement the design. One of the most novel design elements was elimination of the use of sheath fluid, which is used to focus the particles. Cytometry requires particles to travel at a single file line and/or at consistent speed; otherwise, overlapping and clumping of the particles can cause inaccurate results. Most current commercial cytometry products achieve this with hydrodynamic focusing [2]. Hydrodynamic focusing works by injecting a stream of particles and fluid into a larger, already flowing stream of fluid of different density and velocity, known as the sheath fluid (all of this is discussed in greater detail below) [2]. Because this requires the coordination of two separate pumping systems, it adds greatly to the complexity and cost of the flow cytometer. Communication with the project sponsor established the desirability of pursuing a different method for achieving a constant particle speed [3]. Additionally, one of the

methods by which the sponsor intended to cut costs was the use of a replaceable flow cell, which would prevent the need for a dedicated cleaning system to sterilize the cell after each run but would also prevent the use of any fluid control system such as hydrodynamic focusing which requires a fixed flow cell.

Background research and conversation with the sponsor established the desirability of pursuing a focusing method that utilized inertial microfluidics, which harnesses the natural behavior of fluid flow in order to direct and guide the particles. However, inertial microfluidics is an emerging field, and the behavior is still not fully understood. For this reason, computational fluid dynamics (CFD) simulation was performed in order to predict the behavior of particles flowing through a cytometer and whether these results could be observed to conform with empirical results from previous research.

2 Background

Flow cytometry is a rapidly growing field with many advantages for medical and biological science. However, the majority of current systems are large, expensive, and complicated to operate, which limits their availability to point-of-care or resource-limited settings such as academia or smaller companies [4]. These issues are driven by the high fixed and operating costs of flow cytometers (often exceeding $30,000 for the cytometers alone), lack of portability, and the requirement to have special training to operate [4]. As a result, there have been several commercial efforts to develop simplified, portable cytometers, such as the Guava EasyCyte, the Partex CyFlow, and the Accuri C6 [5]. In most of these systems, however, the simplification involved "miniaturizing light sources, data acquisition systems, and detectors [5]." Little work has therefore been done on implementing a novel simplified method for sample stream focusing beyond the hydrodynamic focusing that dominates the industry.

2.1 Hydrodynamic focusing

Hydrodynamic focusing uses a separate particle-free fluid known as sheath fluid to constrain and direct the inner sample fluid [2]. The process is initiated by injecting a stream of fluid containing the particles of interest into the sheath fluid, a larger surrounding flow of different speed and density than the internal fluid [2].

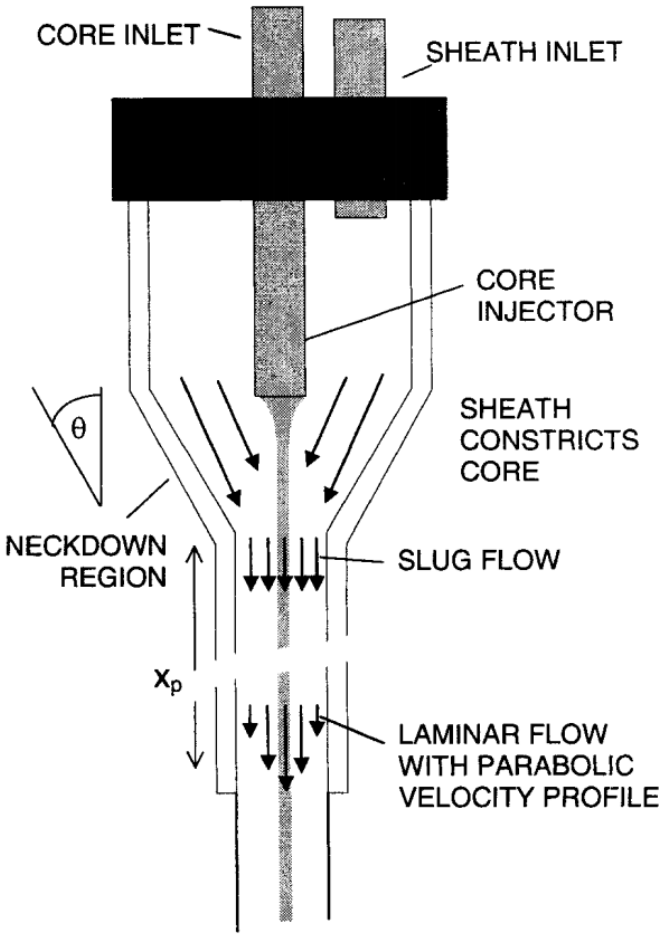

Figure 1: Hydrodynamic focusing using sheath flow, taken from Practical Flow Cytometry by Shapiro [2].

This is done in order to achieve stationary, or streamline, flow, which signifies a constant flow velocity at any given point in the system [2]. However, across the entire cross section of the tube, the flow velocity will not be constant, owing to the effects of viscosity [2]. Friction at the walls means that the fluid particles there will be essentially stationary [2]. The effects of this slowing continue away from the walls, ultimately resulting in a horseshoe-shaped parabolic velocity profile, with minimum velocity at the walls increasing to a maximum velocity in the center of the channel [2]. This phenomenon of flow with a parabolic velocity profile is known as Poiseuille flow [6].

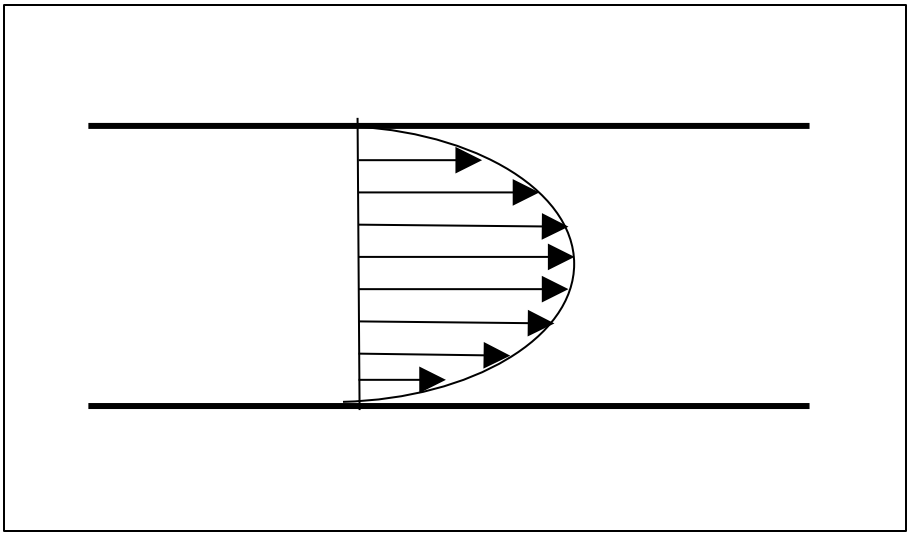

Figure 2: Cross-sectional side-view of a Poiseuille flow velocity profile. The magnitude of the arrow corresponds to the magnitude of fluid velocity at that location in the channel.

To ensure the randomly distributed particles aren't traveling at different speeds because of their different locations in the channel, the cross sectional diameter of the pipe is gradually decreased until the particles are travelling single file [2]. By the principle of conservation of mass, the average velocity of the stream will increase, so care must be taken to not pass from the laminar regime (the fluid flows as if stacked in smooth layers) to the turbulent regime (the fluid becomes disturbed and crosses back on itself) [2].

Another way hydrodynamic focusing avoids the issues associated with the varying velocity of a parabolic flow profile is by harnessing the effects of slug flow [2]. When the cross section of the tube through which a fluid is flowing decreases, it takes time for the effects of friction and viscosity to slow down the edges of the flow and permeate this slowing through the rest of the channel [2]. For this reason, the entrance of a differently-sized pipe demonstrates a region where the flow has not yet changed from approximately constant velocity to the varying velocity of the parabolic profile [2]. This distance from the entrance until the parabolic profile is fully developed known as the development length [2]. In this region, the velocity differences at different points along the axis can be considered minimal [2].

Despite its widespread use in flow cytometry applications, hydrodynamic focusing has numerous downsides that exacerbate the issues of size, complexity, and cost mentioned previously. Hydrodynamic focusing has no way to control the spacing between particles, which limits the maximum detection rate owing to the need to keep the overall flow rate

low enough to prevent particle coincidence or turbulence [5]. Another issue is the tendency of particles to quickly diffuse out of the focused flow; for instance, Zhao et. al. give a time of 3 milliseconds for nanoscale vesicles to diffuse out of a 500 nanometer flow [7]. Finally, the main issue with hydrodynamic focusing is the complexity of the sheath flow process, which requires a separate pumping system, feedback control to ensure a constant flow rate, and the need to keep replacing the sheath fluid [7]. All of this adds to the cost and size of the cytometer.

2.2 Alternate focusing methods

While not in commercial use, researchers have identified several other methods of focusing particle flow in microfluidic applications. These include inertial, hydrophoretic, acoustic, magnetic, optical, electrokinetic, electrophoretic, and dielectrophoretic [8]. Acoustic, magnetic, optical, and electrokinetic and electrophoretic focusing all function similarly, in that some external field is applied to the particles in order to direct and focus their location [5, 8]. Of the remaining methods, hydrophoretic focusing and inertial focusing share the advantage of not requiring additional power beyond that required to pump the sample fluid [5, 9]. However, hydrophoretic focusing, which uses the effects of hydrodynamic interaction between obstacles in the flow channel and the particles in order to direct their motion, requires manufacturing complicated flow cells and leads to the possibility of clogging [9]. Inertial focusing can be induced in much simpler shaped channels without the introduction of obstacles. Given the project requirement to have a simplified design and a disposable flow cell, the decision was made to pursue inertial focusing as the desired method.

2.3 Inertial focusing

Inertial focusing is a passive method in that particle motion is directed and focused by taking advantage of the effects of naturally occurring lift forces acting on particles moving in Poiseuille flow [5]. An additional advantage of inertial focusing is longitudinal spacing due to hydrodynamic repulsion, which can reduce particle coincidence and improve the accuracy of analysis [5]. As yet, no commercial cytometry application has used inertial focusing, which makes it a promising avenue for exploration given its simplicity relative to other methods [10]. Oates et al. performed a proof of concept using inertial focusing in which the focused particle stream was observed to have a coefficient of variation (a

measure of how accurately the cytometer is detecting the data) comparable to commercial products [5].

Inertial focusing as a phenomenon is still not fully understood, and a fully satisfactory theoretical basis for its occurrence remains to be determined. Inertial focusing, or more specifically the "migration of rigid particles (due to lift) across undisturbed streamlines," was first observed experimentally in 1962 by Segre and Silberberg [10]. When passing fully dispersed neutrally- buoyant millimeter-scale particles through a 1 cm diameter cylindrical pipe, they observed the particles migrating towards a ring with a diameter 0.6 times the diameter of the pipe itself [11]. This effect of increasing particle concentration at the radial location of this annulus and decreasing particle concentration everywhere else was termed the "tubular pinch" effect, also known as the Segre-Silberberg effect [11]. The development of this effect was determined to be proportional to the length of the tube, the velocity of the flow, and the fourth power of the ratio between the particle radius and tube radius [11]. Further experiments by other researchers confirmed that the behavior of particles migrating to specific streamlines in a channel also occurs in microscale flows, beyond just the macroscale flows of Segre and Silberberg's initial experiments [12]. Han et al. confirmed that inertial focusing is a robust phenomenon, occurring not only at low concentrations but also at volume concentrations of at least $\varphi = 0.2$ [13]. The annulus equilibrium positions observed by Segre and Silberberg and others appear only in straight circular channels. Different behaviors occur in different flow geometries, and these are discussed in Section 2.3.2.

Beyond the low Reynolds number regime pioneered by Segre and Silberberg, Matas et al. have performed experiments studying microscale particle migration at Reynolds numbers up to 1,700 [13]. As the Reynolds number increased, the equilibrium position was observed to expand outwards [13]. Past *Re* equal to 600, the novel observation was obtained of a second inner annulus that formed around $r = 0.5R$ [13]. This annulus was less tightly constrained than the original Segre-Silberberg annulus, and particles fell in a range between $r = 0.3R$ and $r = 0.7R$ [13]. The limitations of the experimental design meant that it remains unknown whether this inner annulus represents an actual equilibrium point or simply a location of slow particle migration speed [13]. However, given that the density of particles was observed increasing at this inner annulus relative to the outer annulus with increasing Reynolds number, Matas et al. suggest that this provides evidence for a secondary equilibrium location [13].

In addition to migration to equilibrium positions, particles in an inertially focused scenario have been observed to migrate to even longitudinal spacing, in both single-file trains and staggered double-file trains [10]. Di Carlo et al. state that this even spacing occurs for particle Reynolds numbers between ~0.94 and ~1.87 [4]. Below R_P of 0.25, focusing does not occur, while above R_P of 4.68, spacing breaks down and particles begin taking random longitudinal positions [4]. Oates et al. have observed that increasing the particle concentration results in a more tightly focused equilibrium shape [5]. They suggest that this concentration dependence imposes "a lower limit on sample concentration [5]."

2.3.1 Inertial focusing theoretical work

The focusing behavior first observed by Segre and Silberberg was surprising for several reasons. This was the first time direct observation of particles independently crossing streamlines in laminar flow was observed (in laminar flow, each individual fluid element follows a straight parallel streamline) [11]. Stokes flow or creeping flow refers to flow when the effects of inertial forces can be neglected relative to the viscous forces in a flow [13]. In such a case, the simplified Stokes equations prohibit lateral migration of a solid particle [13]. Therefore, as demonstrated by Bretherton, such cross-streamline motion can only be explained by considering the effects of inertia [14]. Indeed, experiments at vanishingly small Reynolds numbers (i.e. with negligible inertial effects) have not shown particles crossing streamlines [15]. Oakey et al. found that in a 30 μm x 50 μm rectangular channel, a 10 μL/min flow rate did not result in focusing behavior while flow rates of 20-100 μL/min did (a 100 μL/min flow rate in this size channel corresponds to an average flow velocity of 1.1 m/s) [5].

At the time of the Segre and Silberberg experiments, the only theoretical basis for inertial migration of a particle came from Rubinow and Keller, who modeled the Magnus effect on a rigid sphere in a uniform flow [13]. By solving the equations of motion for a spherical particle in a parabolic flow, they were able to demonstrate that such a particle would be subjected to both a moment and a longitudinal force [11, 13]. This can be understood as the flow around a particle accelerating more in the gap between the particle and the wall than above the particle [16]. This explained why particles near the wall would experience a centripetal force [11]. However, it did not explain why the particles would not keep traveling centripetally until reaching the central axis. This implied the existence of some undiscovered centrifugal force which balanced with the centripetal force at $r = 0.6\ R$.

Comparable experiments with non-neutrally buoyant particles were performed by Eichorn and Small in 1964 and Jeffrey and Pearson in 1965 [17]. These experiments demonstrated that non-neutrally buoyant particles will migrate towards the channel walls when they lead the flow and migrate towards the central axis when they lag the flow [17]. In 1965, Saffman approximated a solution to the Navier-Stokes equations using the method of matched asymptotic expansions and predicted a laterally-acting lift force which would explain this migration behavior in non-neutrally buoyant particles [13].

Further theoretical work was performed by Ho and Leal, who solved the forces on a rigid particle in a shear flow at small Reynolds numbers using a method of regular perturbations [13]. This was later expanded by Asmolov and others up to Reynolds numbers of 1,500 [13, 16]. Their work suggested that the inertial lift force which causes particles to cross streamlines (as opposed to the viscous drag force which causes particles to stay along streamlines in accordance with Stokes flow) has two components [18, 4]. The first is a wall-induced lift force, which acts centripetally on the particle [18, 4]. This force is believed to be caused by the asymmetric wake of a particle near the wall [19]. As vorticity is generated on the particle surface, the presence of the wall prevents it from being symmetrically distributed in the wake [16]. This wall lift has been observed to become very strong at Reynolds numbers above 100 [16]. The second is a shear-induced lift force, by which the decreasing shear gradient of a parabolic flow profile induces centrifugal motion in the particle [18, 4, 19]. There is of course a secondary drag force counteracting the lateral lift-induced motion of the particle (as opposed to the main drag force counteracting the longitudinal motion) which is discussed below [20].

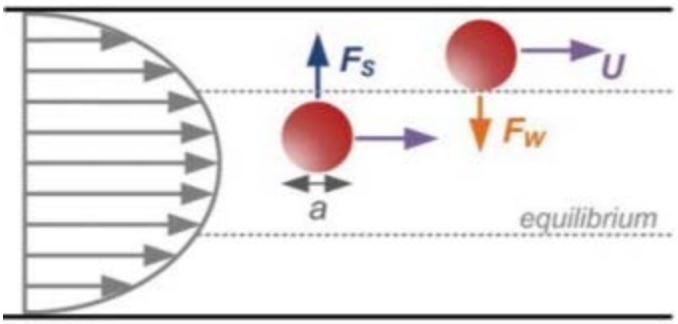

Figure 3: Diagram indicating the direction of action of the two competing lift forces in Poiseuille flow, taken from Zhou and Papautsky [18]. F_s corresponds to the centrifugal shear-induced lift force, F_w corresponds to the centripetal wall-induced lift force, U corresponds to the direction of fluid velocity, a corresponds to the particle diameter, and the gray dotted line corresponds to the equilibrium position.

It was theorized that the balance of these forces results in the particle equilibrium position at $r = 0.6R$ observed by Segre and Silberberg [13]. The lateral motion of a particle can thus be described by the sum of the net lift force and the Stokes drag [13]. Zhang et al. state that the effects of diffusion can be neglected in microfluidic applications [20].

Recent experiments by di Carlo et al. have demonstrated that the magnitude of the net lift force depends on the particle location within the channel [18]. Near the centerline, the vorticity around the particle surface causes the centrifugally-acting shear-induced lift force to predominate [18]. Numerical solutions indicate that this force scales proportionally with the particle diameter [18]. Near the walls, a centripetal lift force dominates [18]. Williams et al. suggest that this force scales proportional to the third power of the particle diameter [18]. This change of the lift force scaling depending on the location in the channel corresponded with the theoretical prediction of a balancing of two different forces by Ho and Leal and Matas et al [10]. Experimental results by Zhou and Papautsky have demonstrated that particle migration is not uniform [18]. This is because the shear-induced lift force is dependent on the second power of the shear rate [18]. As a parabolic velocity profile results in a rapidly changing shear rate, the particles accelerate laterally in a quadratic fashion [18]. As they approach the walls, this velocity then decreases exponentially due to both the increase in the drag force as well as the increasing effect of the wall-induced lift force [18]. Experiments by Matas et al. demonstrate that the particles

in the area near the wall are focused much faster (by up to an order of magnitude) than those in other regions [13].

Later experiments demonstrated that the net lift force scaled proportionally to the diameter of the particle [18]. To account for this variation theoretically, Asmolov suggested a non-dimensional lift coefficient C_L, such that the net lift force

$$F_L = C_L G^2 \varrho a^4 ,$$

where G is the shear rate, ρ is the fluid density, and a is the particle diameter [13, 18, 21]. This lift coefficient has been observed to decrease with increasing Reynolds number [18]. Experimentally, the coefficient has been observed to vary between 0.02 and 0.5 [10]. Bhagat et al. state that for most microfluidic applications, the average lift coefficient stays approximately constant at ~0.5 for Reynolds numbers less than 100 [21]. The shear rate is defined as

$$G = 2U_f / D_h ,$$

where U_f is the average flow velocity and D_h is the characteristic length of the channel (given here as the hydraulic diameter, but e.g. the narrowest side length in a rectangular channel) [21]. Substituting this into the equation for lift force gives

$$F_L = \frac{4\varrho C_L U_f^2 a^4}{D_h^2} .$$

Thus, the lift force increases with increasing fluid density, flow velocity, and particle size, and decreases with increasing channel dimensions. This lift force is counteracted by Stokes drag,

$$F_D = 3\pi\mu a U_L ,$$

where μ is the dynamic viscosity and U_L is the lateral migration velocity [21]. By balancing these two force terms, the lateral migration velocity can be solved for as

$$U_L = \frac{4\varrho C_L U_f^2 a^3}{3\pi\mu D_h^2} .$$

This equation can then be used to determine the critical channel length required to fully focus particles. Papautsky et al. derive

$$L_F = 3\pi\mu D_h^2 L_m / 2\varrho U_f C_L a^3 ,$$

where L_m is the particle migration distance [18, 21]. Alternately, di Carlo et al. derive

$$L_F = \pi\mu W^2 / \varrho U_m a^2 C_L ,$$

where W is the width of the channel in the direction of particle migration and U_m is the maximum fluid velocity ($U_m = 2U_f$) [4, 10]. In practice, however, these equations have not been observed to model focusing length completely accurately [18]. For this reason, it has become common to use the equation to make an estimate and then overengineer the device by making the channel longer than predicted [18].

The relationship between the Reynolds number of the flow and the lift force is more complicated than at first glance. As the average flow velocity U_f increases, the Reynolds number also increases. However, the lift coefficient is known to decrease with increasing Reynolds number [18]. This means that each situation will have some optimal Reynolds number that results in minimum critical focusing length [18].

Matas et al. conducted numerical simulations to determine whether the theoretical model matched with their experimental results [13]. Qualitatively, the appearance of the simulation annulus did match the experimental annulus; however, the simulation showed a much higher density of particles along the annulus than was observed in reality [13]. The simulation results also point to the emergence of an inner annulus at Reynolds numbers above 600 [13]. Again, the simulated annuli show much greater particle density than was observed in reality [13]. As mentioned previously, it is unknown whether this inner annulus represents a genuine new equilibrium position or just the side-effect of a local minimum in the concave force profile resulting in a slowly-moving patch of particles that would migrate away given more time [13]. According to Matas et al, the observed independence of particle distribution relative to particle size (i.e. the same fraction of particles appears in the inner annulus with both large and small particles, despite the inverse relationship of particle diameter and lift coefficient) implies that the inner annulus is a genuine equilibrium point and not a temporary feature [13]. However, the theoretical lift-force balance discussed previously cannot explain the emergence of a secondary equilibrium position. To explain this discrepancy, Matas et al. suggest the failure of the point-particle assumption, a difference between the geometry of the model and the experiment, or both [13]. As mentioned below, the focusing behavior does depend on the assumption of axisymmetric particles, and focusing behavior was observed to be different for non-spherical particles. According to di Carlo, future theoretical models must also take into account the variation of lift force with Reynolds number, the neglected effects of cell deformation on lift force, and interparticle forces [10].

2.3.2 Inertial focusing in asymmetric channels

The balancing of two lift forces can satisfactorily explain the focusing behavior of particles in a cylindrical pipe, but non-radially symmetric pipes exhibit more complex behavior which require the introduction of new forces [18]. In square channels, particles focus to four distinct equilibrium positions, one aligned with the center of each face [4]. Increasing the channel face aspect ratio to a rectangle removes the unstable positions on the short faces, leaving only the positions aligned with the long faces [4].

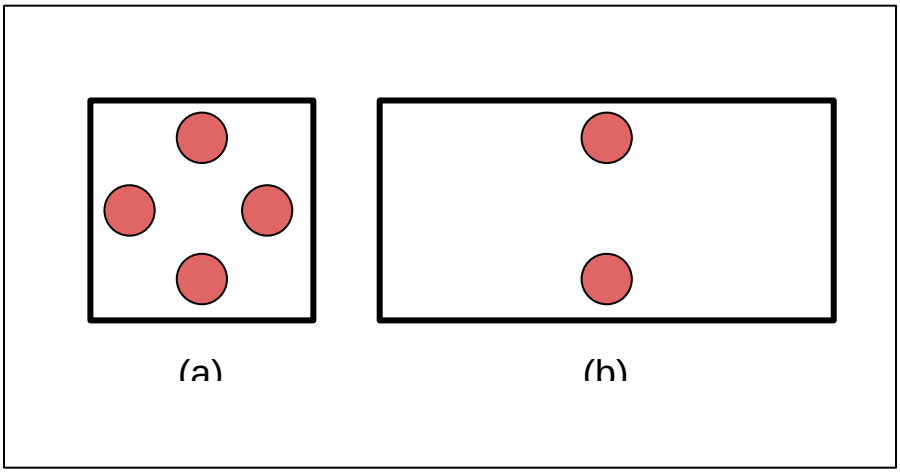

Figure 4: Head-on view of particle equilibrium positions in (a) square and (b) rectangular channels.

Focusing behavior is observed as long as the ratio of particle size to hydraulic diameter a/D_h > 0.07 [18]. There have been inconsistencies with these results, however; some parties have reported eight separate equilibrium positions in square channels, rather than four [18]. The net force expression can be used to estimate the equilibrium positions in a rectangular channel by defining the hydraulic diameter as

$$D_h = \frac{2WH}{W+H},$$

where W is the width (longer dimension) and H is the height (shorter dimension) [18]. This formulation, however, would predict particles focusing at the corners of the channel, down the shear gradient, rather than in the center [18]. Zhou and Papautsky have observed temporary "sidestreams" forming at the corners of rectangular channels, but these are temporary local force minima and not stable equilibrium positions [18].

The existence of these equilibrium positions at the center of side walls in rectangular channels implies the existence of an additional "positive" lift force, induced by

particle rotation, that impels the particles against the velocity gradient in a channel [18]. Such positions cannot be explained by just the "negative" lift discussed above, which impels particles along the velocity gradient [18]. Theoretical work by Saffman suggested that positive rotational lift is an order of magnitude smaller than shear-induced negative lift [18]. This was confirmed experimentally by Zhou and Papautsky, whose results also corresponded with the numerical predictions of Kurose and Komori [18]. However, these experiments did indicate that rotation-induced lift becomes significant near the wall [18]. Thus was established a relationship for the positive lift coefficient

$$C_L{}^{+} \in \frac{H^2}{a\sqrt{Re}},$$

where *H* is the height (i.e. the length of the shorter side of the rectangle) and *Re* is the Reynolds number [18]. By this model, inertial focusing in rectangular channels occurs in two stages: a first rapid stage, in which the particles move towards the walls, and a second slower, rotation-lift dominated stage in which particles move along the walls towards their final equilibrium positions [18].

Inertial focusing is complicated in curved channels by the introduction of the effects of Dean flow [10]. Dean flow is a phenomenon that arises in curved channels because of the difference in velocities between the inside and outside of the curve [10]. Fluid elements near the channel centerline have the highest inertia and thus flow centrifugally relative to the curve of the channel, which creates a pressure gradient [10]. To accommodate the motion of this fluid, the slower fluid near the wall is pushed out of the way, both up and down, and ends up recirculating [10]. Thus, flow in a curved channel results in two symmetric vortices about the centerline [10, 5]. The magnitude of this secondary flow is described by the dimensionless Dean number

$$\varkappa = \sqrt{H/2R} \cdot Re\,,$$

where *H* is the channel dimension in the plane of the curve, *R* is the radius of the channel curve, and *Re* refers to the Reynolds number of the channel [10]. Because particle focusing is independent of particle density, di Carlo et al. state that the symmetry reduction in curved channels cannot be explained by a centrifugal force alone and must therefore be affected by a Dean force of similar magnitude [19]. They propose that the behavior of particles can be modeled as a superposition of the effects of inertial lift and Dean drag [10]. When these two forces are approximately equivalent, it results in modified equilibrium positions for the particles, as opposed to the original equilibrium positions of inertial lift alone or the

recirculating secondary flow that would be expected from Dean flow alone [10]. This secondary Dean flow can also appear if there are obstacles in a straight channel [20].

As the aspect ratio of a rectangular channel increases, the velocity profile becomes wider and flatter, which decreases the shear gradient and thus the shear-induced lift force [22]. The wall-induced lift force is also affected by a changing hydraulic diameter, but the effect is small enough to be neglected in most cases [22]. Finally, the Dean drag increases with increasing width [22].

Di Carlo identifies several advantages to the use of curved inertial focusing, including a reduction in the total number of equilibrium positions and a reduction in the length of channel required for total focusing [10]. Using curved or straight channels alone has not been able to focus particles to a single streamline [5]. However, Oakey et al. have achieved focusing to a single streamline by combining asymmetrically curved channels with high-aspect ratio straight rectangular channels in series [5]. Some researchers have also achieved single streamline focusing by utilizing non-Newtonian fluids. For example, Lim et al. have adjusted the viscoelasticity of the sample fluid by adding micromolar concentrations of hyaluronic acid [12]. This resulted in particle focusing to a single stabilized streamline in the center of the cross section as opposed to the four equilibrium points observed in Newtonian fluids (usually water) [12]. Newtonian fluids such as water typically have negligible elasticity [12]. Because shear-induced and rotation-induced lift only explain the multiple equilibrium positions mentioned previously, Lim et al. propose that the migration towards the centerline is induced by gradients in the normal stress differences that occur when the shear rate in a viscoelastic fluid varies about the particle.

Matas et al. noted that non-spherical particles behaved differently than spherical particles and did not focus as cleanly as the others [13]. Luckily, this deformation appears to be related to the fact that the spherical particles in their experiment were reused for multiple pumpings [13]. As noted by di Carlo, it has been shown that the high shear rates in inertial microfluidic systems are not sufficient on their own to significantly deform biological cells [10]. This is due to the fact that the cells are not fixed, so high shear rates result in high rotation rates rather than high shear stress [10].

2.3.3 Modeling inertial focusing

The field of inertial microfluidics is still developing, and the phenomena are not fully understood. As mentioned above, simulations such as those conducted by Matas et al. based

on the net lift theoretical framework still do not fully correspond with empirical observations [13]. Several recent attempts have been made to more accurately model the behavior of inertial focusing using computational fluid dynamics (CFD). CFD works by modeling a fluid geometry as the sum of numerous smaller, simpler fluid elements, and then iteratively solving the partial differential equations (PDEs) that describe the state of the fluid [23]. These efforts are summarized in Table 1 and are discussed in more detail below.

Table 1
A chronological summary of inertial focusing modeling efforts

Model	Method	Description	Validation
Feng et al. (1994)	Finite element method	2D particle motion in Poiseuille flow using semi-implicit FEM on triangular unstructured grid	Comparison to empirical results
Hu & Zhu (2000)	Arbitrary Lagrangian-Eulerian	3D motion of single particle in Poiseuille flow using an arbitrary Lagrangian-Eulerian moving mesh	Comparison with other simulations
Yang et al. (2005)	Distribution of Lagrange multipliers	3D motion of single particle using fictitious domains to solve continuity equations and DLM to solve rigid-body motion	Comparison with other simulations
Bhagat et al. (2008)	Finite element method	3D particle motion in curved rectangular channel using	Conducted experiment
Prohm et al. (2012)	Multiple-particle collision dynamics	3D particle motion using FEM for fluid flow and particle collision for particle motion	Comparison with empirical results and other simulations
Guan et al. (2013)	Numerical simulation	Numerical simulation of 3D particle motion in curved rectangular channel	Comparison with empirical results
al-Amin (2015)	Discrete phase model	3D particle trajectory tracking in curved rectangular channel	Conducted experiment

Through the 1990's, progress was made on simulating two-dimensional particles in Poiseuille flow, but the results did not always match those from empirical work [24]. Earlier attempts by Feng et al. had demonstrated that qualitatively speaking, two-dimensional simulations can usually match the results of three-dimensional simulations, but not perfectly and run the risk of developing serious unnoticeable errors [25]. In 1994, Feng et al. simulated the motion of a two-dimensional particle in Poiseuille flow using a semi-

implicit finite element method on a triangular unstructured grid with the Polyflow program [25]. A finite element method is a scheme in which the function space is broken down into a grid of cells [23]. In contrast to the finite difference method, this grid need not be structured [23]. The FEM is often more complicated than other methods but also has many advantages for complex geometries and higher order accuracy [23]. The authors found the particles approximately focusing to the Segre-Silberberg equilibrium points [25]. As seen in experimental results, the size of the annulus increased with increasing Re [25]. The effect of particle size was not a major focus of this investigation [25]. However, the researchers' simulations disagreed with the results of experiments for non-neutrally buoyant particles [25]. A lagging particle should migrate to the centerline, but the simulation showed it staying in an annulus, albeit closer to the centerline than the neutrally buoyant annulus [25]. The authors suggest that, based on close examination of experimental trends, if the density difference is small enough, the particle should stabilize near but not at the centerline [25]. A leading particle should migrate to the wall, but the simulation indicates it should get close but stay repelled by a wall force [25]. The researchers suggest that this behavior is more likely accurate and the assumption that a particle will migrate all the way to the wall is an improper extrapolation of experimental trends that does not take into account the degree to which the magnitude of wall-induced lift increases at short distances from the wall [25].

In 2000 Hu and Zhu pioneered the use of an "arbitrary Lagrangian-Eulerian moving mesh" scheme (ALE code) to simulate the motion of spherical particles in three dimensions [24]. In 2005, Yang et al. introduced a competing technique using fictitious domains, in which the continuity equations were solved at all locations, including within the particles [24]. The flow elements within the particles are forced into rigid-body motion by a distribution of Lagrange multipliers, which gives the method its acronym DLM [24]. Yang et al. compared the two competing schemes by simulating the lateral migration of a single neutrally buoyant particle in tubular Poiseuille flow [24]. Both schemes are variations of the finite element method [15]. The ALE code had a typical mesh of 1.46×10^5 nodes while the DLM code used 2.22×10^6 nodes [24]. There was good agreement between the two codes in terms of predicted velocity, but less strong agreement in terms of lift force [24]. In spite of the disagreement, the authors regard the results as acceptable given "the challenging nature of three-dimensional simulation [24]." The ALE code is better suited to solve for lift force because of mesh adaptivity as well as the fact that DLM doesn't explicitly solve for

hydrodynamic forces [24]. Interestingly, the simulation suggests that the centerline is an equilibrium point for particles, but an unstable one [24]. Increasing the Reynolds number of the simulation required a more refined mesh, and also increased the radius of the equilibrium annulus, which matches with experimental results [24]. Comparison with experimental results by Matas et al. showed good agreement [24]. However, the authors were not able to observe the secondary inner equilibrium position that formed at high Reynolds numbers observed by Matas et al [24]. It remains to be determined whether this is a genuine secondary equilibrium position or instead due to some particle interaction during the experiment [24]. The authors also compared the lift correlations from their simulations with analytical lift formulae from the literature [24]. Their correlations changed sign at the Segre-Silberberg radius, which does not occur in the lift formulae [24].

In 2012, Prohm et al. attempted a novel method, multi-particle collision dynamics (MPCD), to simulate the migration of single particles in microchannels at intermediate Reynolds number [15]. Similar to other methods, it numerically solves the Navier-Stokes system but also allows for thermal fluctuations and it is very efficient [15]. MPCD has two steps [15]. First, effective fluid particles are stepped forward according to Newton's equations of motion without any interaction [15]. Then, a correction term is introduced to account for collision, conserving linear and angular momentum [15]. The simulation was also performed in a constrained form in which the particle could only move longitudinally in order to evaluate the generated lift force [15]. The simulation was evaluated by generating a radial probability distribution for particles [15]. The Segre-Silberberg radius was observed forming [15]. As seen in experimental results, the radius increases with increasing Re and decreasing particle size, and the radius gets tighter with increasing Re [15]. In agreement with the simulation by Yang et al., Prohm et al. observed the simulated lift force changing sign at two locations, the centerline and the Segre-Silberberg annulus [15].

In 2008, Bhagat et al. used CFD-ACE+ to validate their design for a spiral microchannel that would separate particles of different sizes [26]. Their model used incompressible laminar flow with the density and viscosity set to that of water (1000 kg m^{-3} and 10^{-3} kg m^{-1} s^{-1}, respectively) [26]. The inlet was set as a flow rate varying from 5 mL min^{-1} to 20 mL min^{-1}, with the outlet set as zero pressure [26]. The particle motion was solved using the SPRAY second-order upwinding scheme [26]. They were randomly dispersed into the inlet at zero input velocity in order to match the speed of the fluid [26].

They also chose to include a diffusion coefficient $D = 10^{-10}$ m^2 s^{-1}, modeled using a second-order limiting scheme [26]. The Algebraic MultiGrid, Conjugates Gradient Squared, and Preconditioning solvers were used to solve pressure, velocity, and species, respectively [26]. Their results were validated in testing by the successful separation of particles in the spiral microchannel [26]. In 2013, Guan et al. reported developing a three-dimensional model in COMSOL to try to match their empirical results focusing particles with a spiral microchannel, with inconclusive results [27]. Their model, of a 120° arc of the channel, used incompressible laminar flow with the density and viscosity set to that of water and no-slip boundary conditions at the walls [27]. The inlet was set as a flow rate varying between 1 mL/min and 8 mL/min, and the outlet was set as zero pressure with no viscous stress [27]. In 2015, al-Amin simulated the effects of inertial focusing in a spiral microchannel with a trapezoidal cross section using the discrete phase model (DPM) in ANSYS Fluent [28]. The DPM method is unique in that it allows the user to directly observe the particle trajectories [28]. The inlet flow condition was varied between 0.1 m/s and 3 m/s, the outlet was set to atmospheric pressure, and the wall boundary condition was set to no-slip [28]. Microscale particles with perfectly elastic collision physics were introduced at every node of the inlet surface [28]. The density difference was negligible, as polystyrene has a density of ~1.05 g/cm^3 [28]. The trajectory of the particles was calculated by summing the forces acting on them [28]. These included the drag force, the buoyant force, and the lift force [28]. The force balance used by Fluent does not include the lift force first derived by Asmolov [29, 28]. Fluent does include an optional term for Saffman's lift due to shear, but this term is only recommended for submicron particles, as it is only valid for situations where the particle Reynolds number due to the particle-fluid velocity difference is smaller than the square root of the particle Reynolds number due to the shear field [29]. For this reason, the lift force was included in the force balance through the addition of a User Defined Function [28]. The coefficient of lift, which varies with Reynolds number and the location of the particle in the microchannel, was determined by generating a polynomial approximation for the average coefficient given different Reynolds numbers [28]. This equation was given as

$$C_L = 3.4368 Re^{-0.714},$$

with the coefficient assumed to approach the constant value of 0.5 for Reynolds numbers less than 15 [28]. This simulation was validated by comparing the particle trajectories to those measured experimentally using a high-speed camera and fluorescent beads, which showed good agreement [28].

While the discrete phase model has thus been used to demonstrate the separation of streamlines for different sized particles in a rectangular channel, it has not been used to demonstrate the emergence of the Segre-Silberberg annulus in a microscale cylindrical channel.

3 Methodology

Based on background research, the goal of this thesis is to simulate the effects of inertial focusing in a microscale straight cylindrical channel which have been observed empirically. These simulations will be performed using the discrete phase model in the ANSYS Fluent program, the same one used by al-Amin for simulating streamline separation in a curved rectangular channel [28]. This section will detail how these simulations were set up and what assumptions were used.

The Lagrangian discrete phase model (DPM) in ANSYS Fluent uses the Euler-Lagrange approach and consists of two components [29]. The fluid is treated as a continuum and solved using the Navier-Stokes equations [29]. The particles are the dispersed phase, and are solved for by tracking their motion through the flow field [29]. They are capable of exchanging momentum, mass, and energy with the fluid phase, which entails a "coupled" or "two-way coupling" approach (this contrasts with an "uncoupled" or "one-way coupling" approach, in which the continuous flow is not impacted by the discrete flow) [29]. The Euler-Lagrange approach is much simpler to solve than the Euler-Euler approach [29]. This approach can only be used when the dispersed phase is a small fraction of the total volume, usually below 10-12%, although the mass fraction may be much higher [29]. This is due to the assumption that particle-particle interactions can be neglected [29]. Modeling particle collisions for higher volume fraction situations requires the use of the mixture model or Eulerian model [29]. The mixture model works by solving the momentum, continuity, and energy equation for the mixture of multiple phases, the volume fraction equations for the secondary phases, and the expressions for the relative velocities [29]. The Eulerian model instead models each phase separately from an Eulerian frame of reference, in contrast with the Eulerian-Lagrangian approach of the DPM [29]. The Eulerian model is more accurate but more computationally expensive, and thus should only be used in complicated cases such as particles of varying sizes [29].

3.1 Solving flow motion (Eulerian)

The motion of the flow is solved using the conservation equations for mass and momentum [29]. The mass conservation equation, or continuity equation, is

$$\frac{\delta \varrho}{\delta t} + \nabla \cdot (\varrho \bar{u}) = S_m ,$$

where the first term is the change in density (goes to zero in incompressible flows), the second term is the divergence of mass flow, and S_m is the mass which is introduced to the fluid element via the motion of the dispersed second (solid) phase [29]. This equation is expanded to three dimensions as

$$\frac{\delta \varrho}{\delta t} + \frac{\delta}{\delta x}(\varrho u) + \frac{\delta}{\delta y}(\varrho v) + \frac{\delta}{\delta z}(\varrho w) = S_m .$$

Conservation of momentum in a non-accelerating frame is described by the equation

$$\frac{\delta}{\delta t}(\varrho \bar{u}) + \nabla \cdot (\varrho \bar{u}\bar{u}) = -\nabla p + \nabla \cdot \tau + \varrho g + F ,$$

where p is the static pressure, τ is the stress tensor, ρg is the gravitational body force and F is the external body force (in this case, the force due to interaction with the dispersed phase). Because the fluid is assumed to be incompressible and constant temperature, the term for energy conservation is neglected [29]. By only considering laminar flows, the complicated stochastic modeling required for turbulent flows is also neglected [29].

The flow is solved with a three-step control-volume technique:

1) Using a computational grid, the domain is divided into a number of smaller discrete control volumes.
2) For each control volume, the governing equations are integrated to generate algebraic expressions for the unknown discrete dependent variables such as velocity, pressure, etc.
3) Each system of equations of unknown variables is linearized and solved [29].

There are two numerical methods to carry out these calculations. The first, a density-based solver, obtains the density field by solving the continuity equation and the pressure field by solving the equation of state [29]. The second, the pressure-based solver, extracts a pressure correction equation from the continuity and momentum equations to solve the pressure field [29]. The pressure-based solver is better suited for incompressible flows, which is why it will be used [29].

3.2 Solving particle motion (Lagrangian)

The discrete phase is simulated by solving the trajectory of each particle by integrating the force balance on the particle [29]. This is the Lagrangian specification which moves with the particle referred to in the name Euler-Lagrange approach, as opposed to the Eulerian specification used to solve the fluid motion [29]. The force balance equation matches the particle inertia with the forces acting on the particle as

$$\frac{\delta \bar{u}_p}{dt} = \frac{\bar{u}-\bar{u}_p}{\tau_r} + \frac{g(\varrho_p-\varrho)}{\varrho_p} + F \ ,$$

where the first term is the drag force per unit mass, the second term is the gravitational force per unit mass, and the final term accounts for any additional accelerations [29]. The variables in the equation are the particle velocity u_p, the fluid velocity u, the particle density ρ_p, the fluid density ρ, the gravitational acceleration g, and the particle relaxation time τ_r [29]. The particle relaxation time is defined as

$$\tau_r = \frac{\varrho_p {d_p}^2}{18\mu} \frac{24}{C_d Re} \ ,$$

where d_p is the diameter of the particle, μ is the molecular viscosity of the fluid, C_d is the coefficient of drag and Re is the relative Reynolds number [29]. The coefficient of drag is defined as

$$C_D = a_1 + \frac{a_2}{Re} + \frac{a_3}{Re^2} \ ,$$

where a_1, a_2, and a_3 are constants defined by Morsi and Alexander that vary over the range of Reynolds values [29]. The relative Reynolds number is itself defined as

$$Re = \frac{\varrho d_p |\bar{u}_p - \bar{u}|}{\mu} \ ,$$

establishing the ratio of inertial forces on the particle relative to the flow to the viscous forces acting on the particle [29]. Particle rotation is solved for with an ordinary differential equation for the particle's angular momentum,

$$I_p \frac{d\omega_p}{dt} = \frac{\varrho_f}{2}\left(\frac{d_p}{2}\right)^5 C_\omega \Omega = T \ ,$$

where I_p is the moment of inertia, ω_p is the particle angular velocity, C_ω is the rotational drag coefficient, Ω is the relative particle-fluid velocity, and T is the torque applied to the particle [29]. The torque is thus caused by the equilibrium between the particle inertia and the drag [29]. The moment of inertia for a sphere is defined as

$$I_p = \frac{\pi}{60} \varrho_p d_p^{\,5} ,$$

while the relative particle-fluid velocity is defined as

$$\Omega = \frac{1}{2} \nabla \times u_f - \omega_p ,$$

where the first term is the curl of the flow velocity vector [29]. The coefficient of rotational drag used by Fluent comes from the correlation defined by Dennis et al.

$$C_\omega = \frac{6.45}{\sqrt{Re_\omega}} + \frac{32.1}{Re_\omega} ,$$

where Re_ω is the rotational Reynolds number

$$Re_\omega = \frac{\varrho_f |\Omega| d_p^{\,2}}{4\mu_f}$$

[29]. The coefficient correlation is valid for rotational Reynolds numbers between 20 and 1000 [29].

The final term F in the force balance equation refers to any additional forces that act on the particle in special situations. If the density of the fluid is much less than the density of the particles ($\rho/\rho_p << 1$), the "virtual mass" (additional inertial term referring to the force required to accelerate the fluid displaced by the particle) and the pressure gradient can be neglected [29]. However, as in this case, when the particle is neutrally buoyant or approximately buoyant and the density ratio tends to unity, these forces are no longer negligible and must be included in the F term. The "virtual mass" term is defined as

$$F_{vm} = C_{vm} \frac{\varrho}{\varrho_p} (\bar{u}_p \nabla \bar{u} - \frac{d\bar{u}}{dt}) ,$$

where C_{vm} is the virtual mass factor with a default value of 0.5 [29]. The pressure gradient term is defined as

$$F_{pg} = \frac{\varrho}{\varrho_p} \bar{u}_p \nabla \bar{u} ,$$

where $\nabla \bar{u}$ refers to the gradient of the fluid velocity [29]. Modeling the effects of inertial lift will require the introduction of a User Defined Function (UDF). In order to obtain meaningful trajectory results for coupled discrete-phase calculations, the particles must be tracked in an absolute reference frame [29].

These particle trajectory equations are solved by stepwise integration over discrete time steps [29]. Integration of the force balance yields the velocity at each point, and

integration of the velocity yields the trajectory. Together, these two integrals form a set of coupled ordinary differential equations.

3.3 Defining geometry

Before the simulation can begin, the domain must be defined and the grid established. The domain(s) are modeled using the Solidworks CAD program and then imported into the Fluent workspace. The length of the cylindrical pipe domain will vary between 2 mm and 20 mm long, with a diameter of 100 μm. These dimensions correspond with the size of pipe used in cytometry applications. Figure 5 depicts an example fluid domain modeled in Solidworks with a length of 2 mm. This domain represents the interior of the pipe through which the fluid and particles will flow.

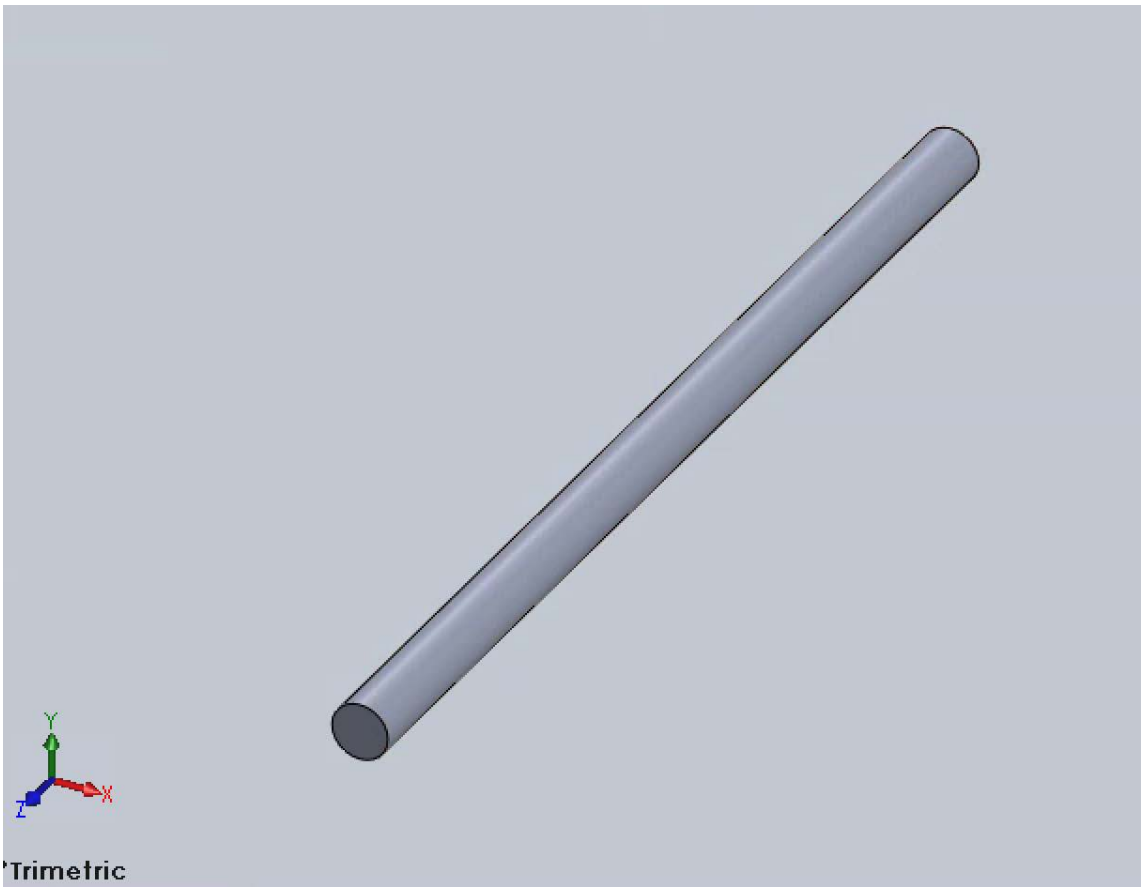

Figure 5: A trimetric view of the flow channel domain in Solidworks.

This geometry was imported into Fluent and three named selections were created from the exterior surface. The circular face closest to the origin along the Z-axis was labeled

Inlet, the circular face furthest from the origin was labeled Outlet, and the remaining wall was labeled Wall.

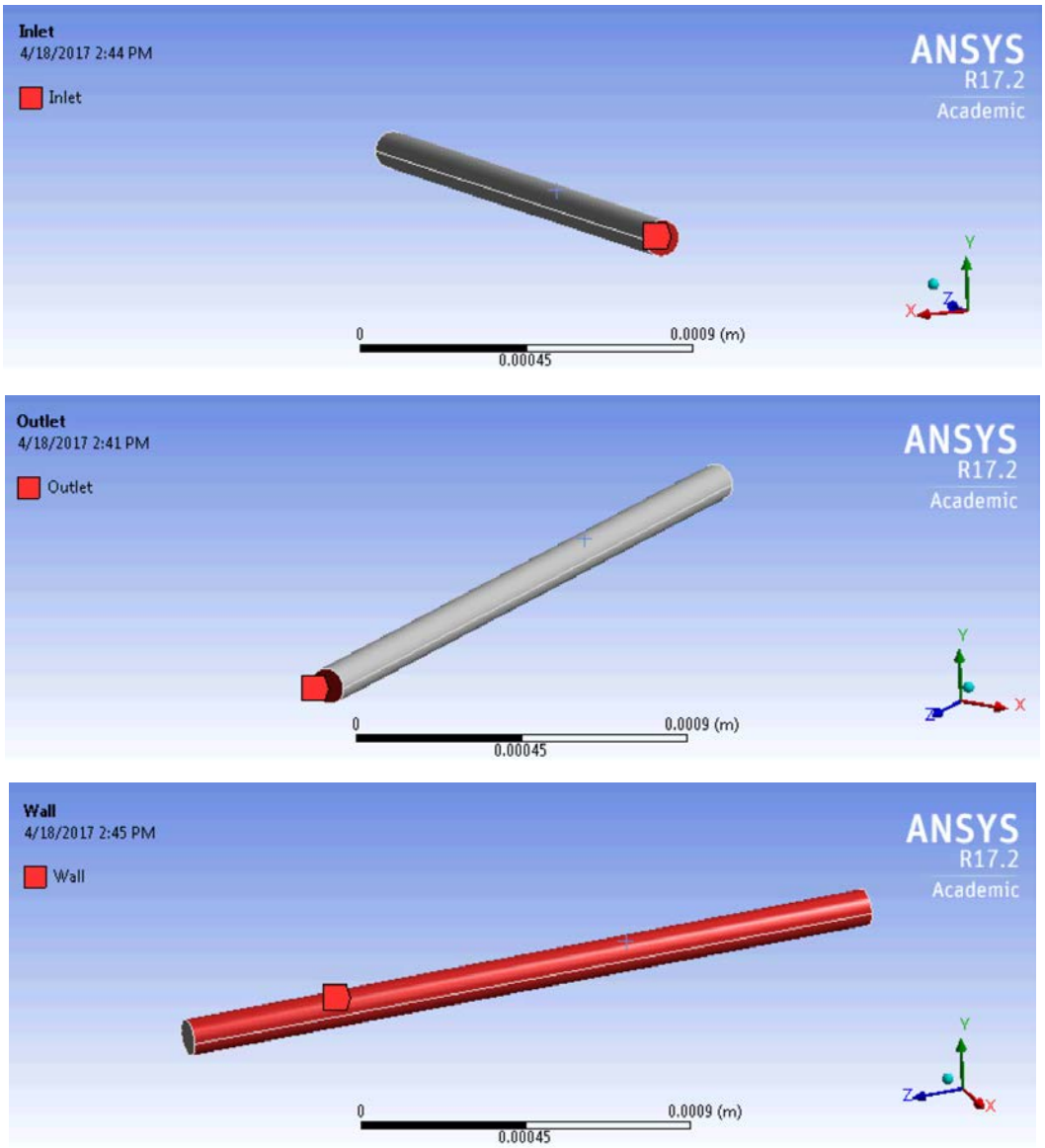

Figure 6: The three different named selections that make up the external surfaces of the domain.

Once imported, a mesh must be generated to divide the domain into a number of smaller control volumes. Meshes can be imported from outside the program, but the Fluent meshing program generates unstructured triangular/tetrahedral meshes for a given 3D geometry [29]. This provides a good balance between computational expense and model quality. The relevance, which controls the fineness of the mesh, is set to 100 for maximum accuracy.

Using the default mesh settings results in the mesh below, with 8763 nodes and 7182 elements.

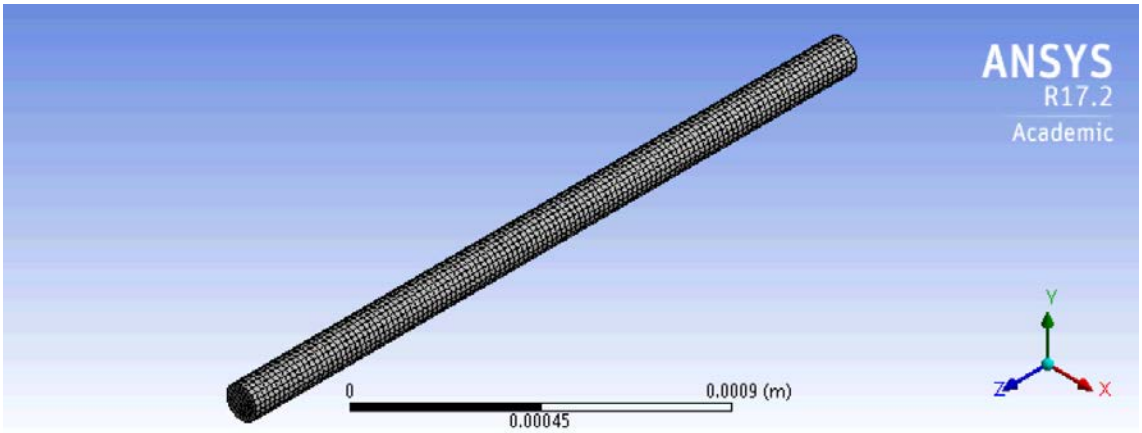

Figure 7: Default mesh on the imported flow channel.

3.4 Initial conditions (fluid)

A full list of assumptions for both the fluid and particle conditions can be found on page 26. The initial conditions are then set for the fluid domain. Double precision is specified in order to obtain more accurate results. The chosen solver is the default, pressure-based with a steady time environment and absolute velocity formulation. The viscous model is left on laminar. The goal of this run is just to model fully-developed laminar flow in a tube, so the discrete phase model is left off. The boundary conditions are set for each named element of the domain. "Inlet" is set as a *velocity inlet* with a velocity magnitude of 1 m/s normal to the surface. "Outlet" is set as a *pressure outlet* with a gauge pressure of 0 Pa, corresponding to atmospheric pressure. "Wall" is set as a stationary *wall* with a no-slip shear condition. The remaining non-surface volume is specified as an *interior* fluid, with the characteristics of water, with a density of 998.2 kg/m^3 and a viscosity of 0.001003 kg/m-s. The temperature is left at the default value of 300 K.

To confirm that this situation will remain in the laminar regime, a calculation is performed using the channel Reynolds number, which is defined as

$$Re = \varrho v D_h / \mu ,$$

where v is the average fluid velocity and D_h is the hydraulic diameter (inner diameter in the case of a circular pipe) [30]. This results in a value of (998 kg/m^3)(1 m/s)(100x10^{-6} m)/(0.001003 kg/m-s) = 99.5. The transition region for laminar to turbulent flow begins at

around Re = 2300, which means that this scenario is well within the laminar flow region [30].

Table 2

List of assumptions used for fluid and particle settings

Laminar flow
Fluid is water (ρ = 998.2 kg/m^3 and ν = 0.001003 kg/m-s)
Velocity inlet, 1 m/s normal to surface
Pressure outlet, 0 Pa gauge pressure
Stationary wall with no-slip shear condition
Constant temperature, 300 K
Particles are evenly distributed at flow inlet
Particles are neutrally buoyant
Particles enter inlet travelling at 1 m/s
Inert particles (no heat transfer or conduction)
No particle interaction
Perfectly elastic wall collisions (coefficient of restitution of 1)

3.5 Solution methods (fluid)

The fluid continuum is solved as streamwise-periodic or fully-developed fluid flow. The default SIMPLE scheme is selected for pressure-velocity coupling. Because a tetrahedral mesh is being used, the flow is not aligned with the mesh because there are no straight grid lines [29]. For this reason, it is important to select second-order accuracy for the discretization. Gradients are evaluated using the default least squares cell based scheme. For spatial discretization, the default schemes of least squares cell based, second order, and second-order upwind are selected for the gradient, pressure, and momentum, respectively. Pressure, density, and momentum use their default under-relaxation factors of 0.3, 1, and 0.7, respectively. The pressure interpolation scheme is set to the default second-order scheme. The density interpolation scheme is the default second-order upwind, which provides good accuracy without being too computationally expensive [29]. Hybrid

initialization is used. The number of iterations is set to 1000, and the simulation is run. After convergence was reached, the simulation was iterated until the residuals stopped changing ("went flat").

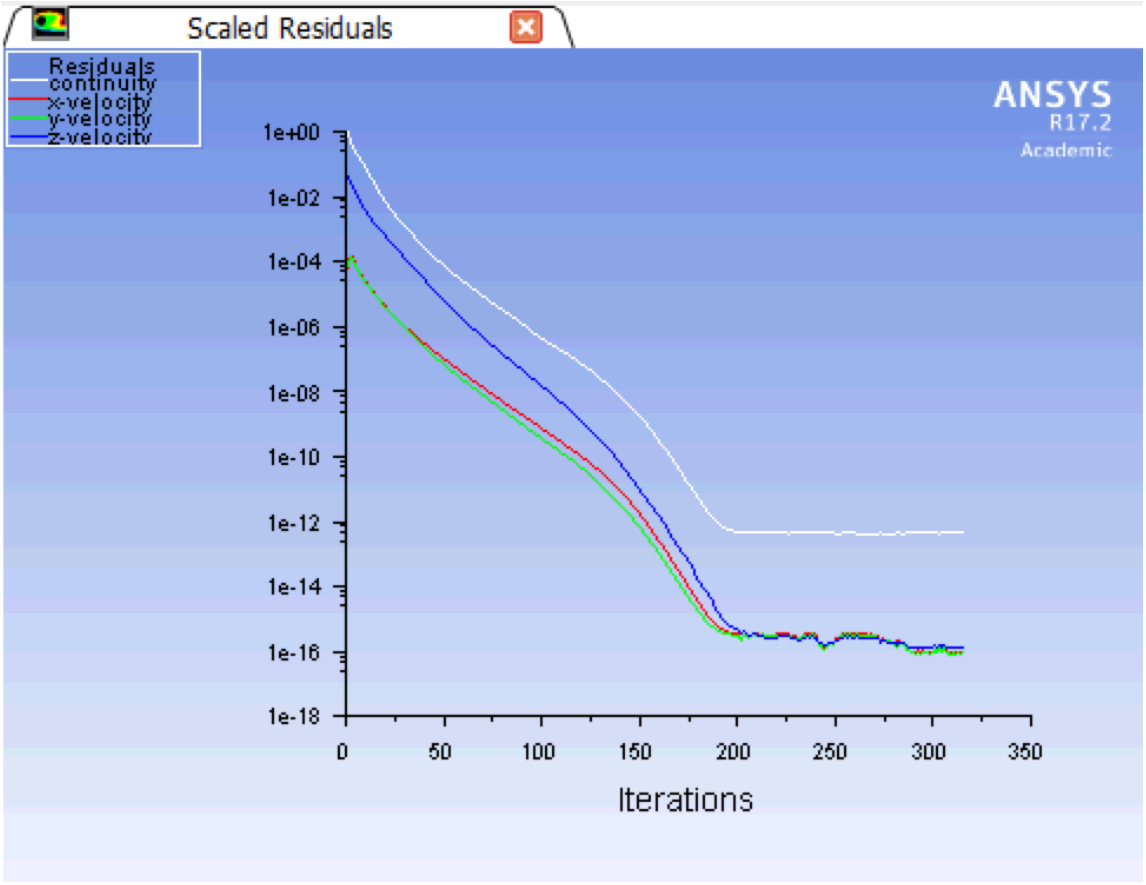

Figure 8: Plot of the residuals, demonstrating how they reach a steady-state.

To confirm that this simulation accurately models the development of laminar flow, the velocity across the outlet diameter was plotted. This clearly shows the parabolic velocity profile characteristic of Poiseuille flow.

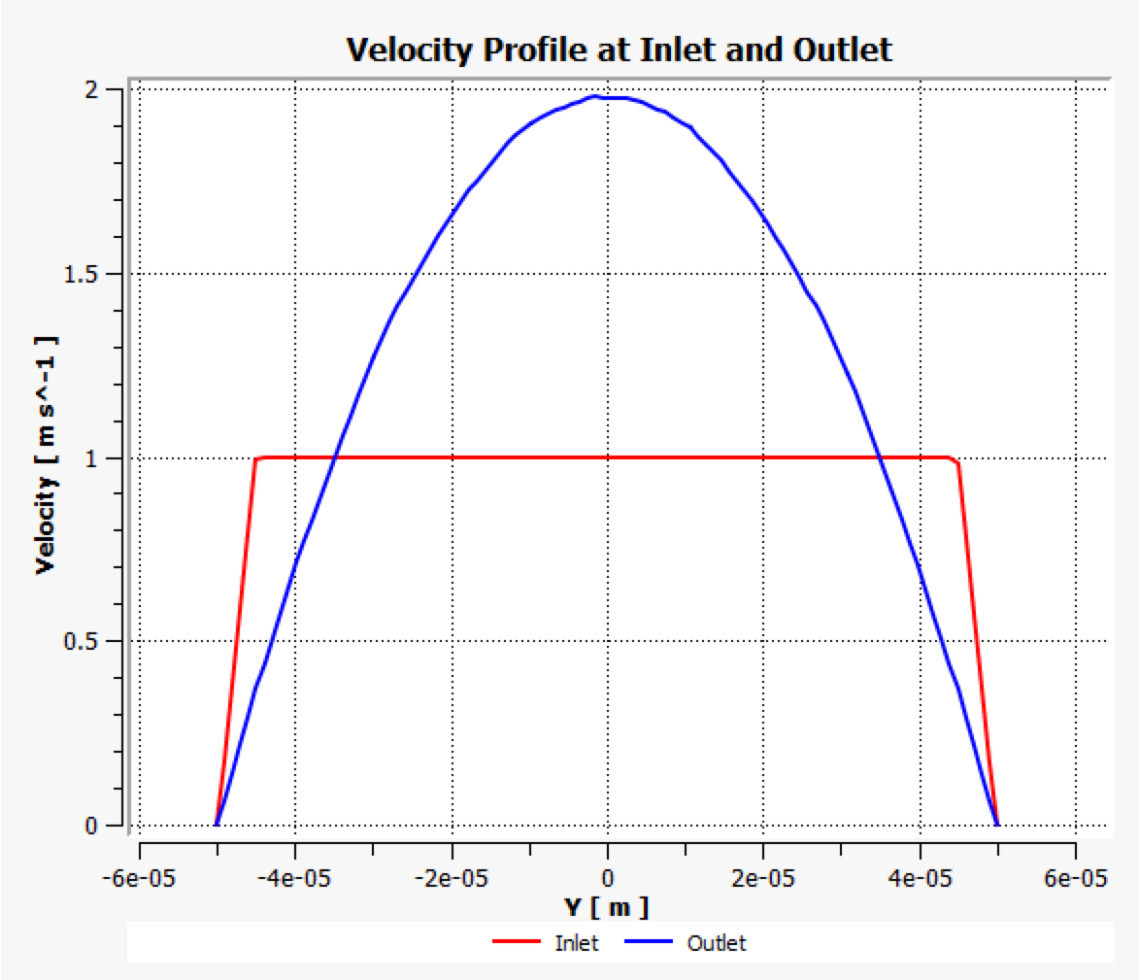

Figure 9: Velocity profiles at the inlet and outlet, showing the continuous velocity profile at the inlet and the parabolic velocity profile at the outlet.

To confirm that this simulation does accurately model the effects of parabolic flow development, the entry length will also be checked. The hydrodynamic entry length for laminar flow, which indicates the length of travel along the channel it takes for a parabolic profile to develop from uniform flow, is defined as

$$L_{h,lam} = 0.05ReD\,,$$

where D is the diameter of the pipe [31]. This results in a value of (0.05)(99.5)(100x10^{-6} m) = 0.4975 mm.

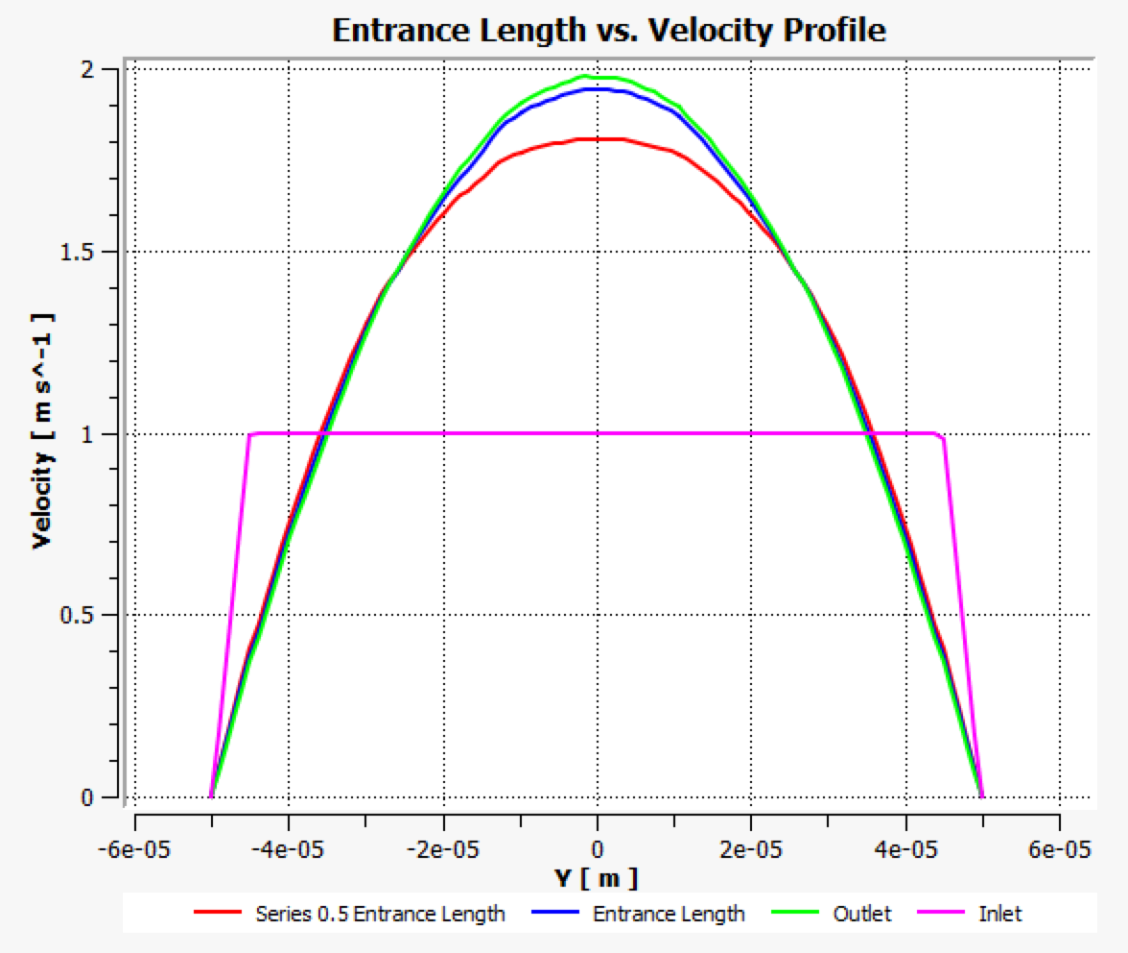

Figure 10: Velocity profiles at different positions along the channel length. There is good agreement between the profile at the entrance length and the fully developed flow at the outlet, which indicates that this simulation is accurately modeling Poiseuille flow.

3.6 Initial conditions (particles)

The next step is to include the discrete phase corresponding to the particles injected into the flow domain. In this case, the particles are assumed to be entering the pipe in a fully distributed state, which requires the use of a particle injection that defines the initial spatial distribution of the particle streams. The particles are assumed to be neutrally buoyant, so they are given the same density as water. The particles are assumed to be traveling at the same velocity as the fluid upon entry (1 m/s). Their diameter will be varied between 1 micron and 10 microns in diameter to observe the effects on focusing of the ratio of particle diameter to channel diameter. As the particles will not experience heat transfer or combustion, the assigned particle type will be inert. Wall boundaries are assumed to reflect a particle with a coefficient of restitution of 1, which makes it perfectly elastic. Inlets and

outlets are assumed to let the particles escape the fluid domain. Additional forces from the F term in the force balance are left untouched, so the only force acting on the particles in this simulation is the drag force (gravity is neglected).

3.7 Solution methods (particles)

This process begins by activating the discrete phase model and specifying interaction with the continuous phase. The DPM is governed by ordinary differential equations, which contrasts with the fluid solutions, which are solved with partial differential equations. By default, the tracking scheme automatically switches between a high-order trapezoidal scheme and a low-order implicit scheme in order to maximize accuracy and stability [29]. In coupled solutions, Fluent applies under-relaxation to the conservation terms in order to decrease the impact of the discrete phase change and increase the stability of the procedure [29]. This under-relaxation factor is by default 0.5. Collisions are neglected, so the particle tracking need not be unsteady. The maximum number of steps to complete a trajectory is left at the default of 50,000. The default step length factor of 5, which indicates to Fluent to adjust the length scale so that the tracking equations update five times over the length of one cell, is left unchanged. Tracking is specified in the absolute frame. The judge for convergence is changed from the default drop in the residuals by three orders of magnitude to one of five orders of magnitude in order to increase the ability of the residuals to reach a steady state.

In the example situation depicted below, a surface injection of inert particles is specified normal to the inlet. The particles are specified to be neutrally buoyant, i.e., having the same density as water. These particles are specified as 5 μm in diameter, injected at 1 m/s. As seen in Figure 11, the lack of inertial forces included in the force balance means that the particles do not cross the streamlines, as expected. As seen in Figure 12, the particles stay dispersed over the cross-sectional area completely over the length of the pipe.

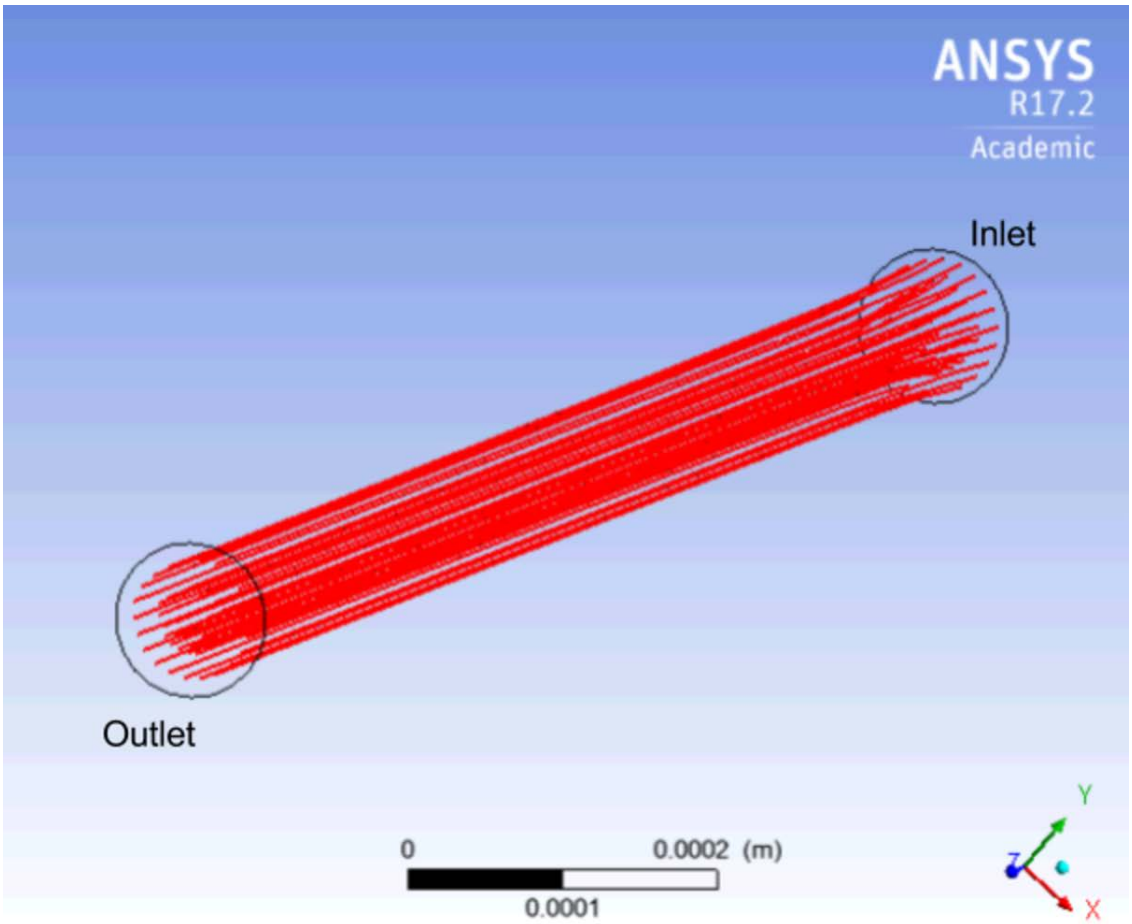

Figure 11: The particle tracks for the simulation with just the viscous forces.

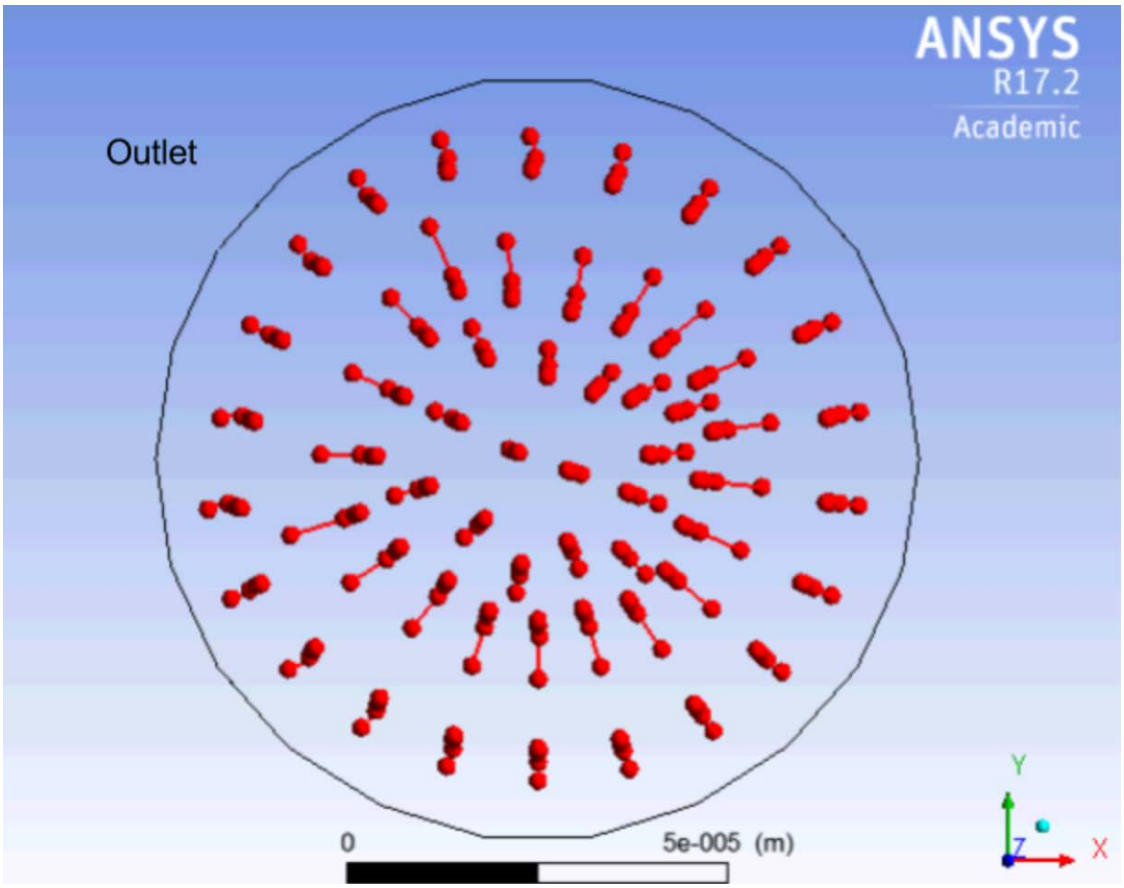

Figure 12: Head-on view of the particle tracks at the outlet.

3.8 Introduction of inertial lift to discrete phase

Next step is introducing the lift force. The first attempt used the algorithm derived by al-Amin [28]. As can be seen in the Figures 13-15, the introduction of the lift force results in focusing behavior. However, it is not symmetrical, nor does it lead to the annulus predicted by experimental results. The asymmetry is believed to be caused by the fact that the current lift formulation only accounts for the magnitude of the force vector and not the sign. Further refinement of the algorithm is needed.

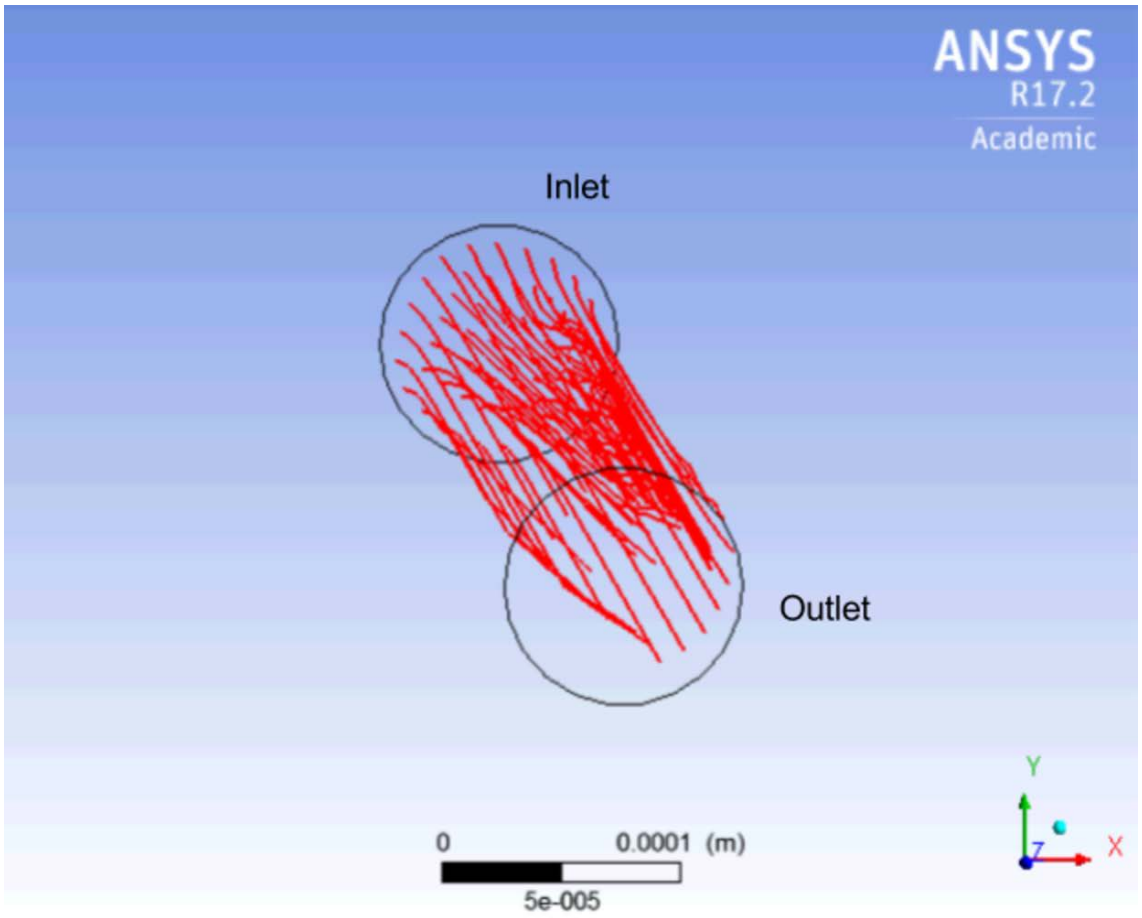

Figure 13: View of particle focusing behavior using the al-Amin algorithm.

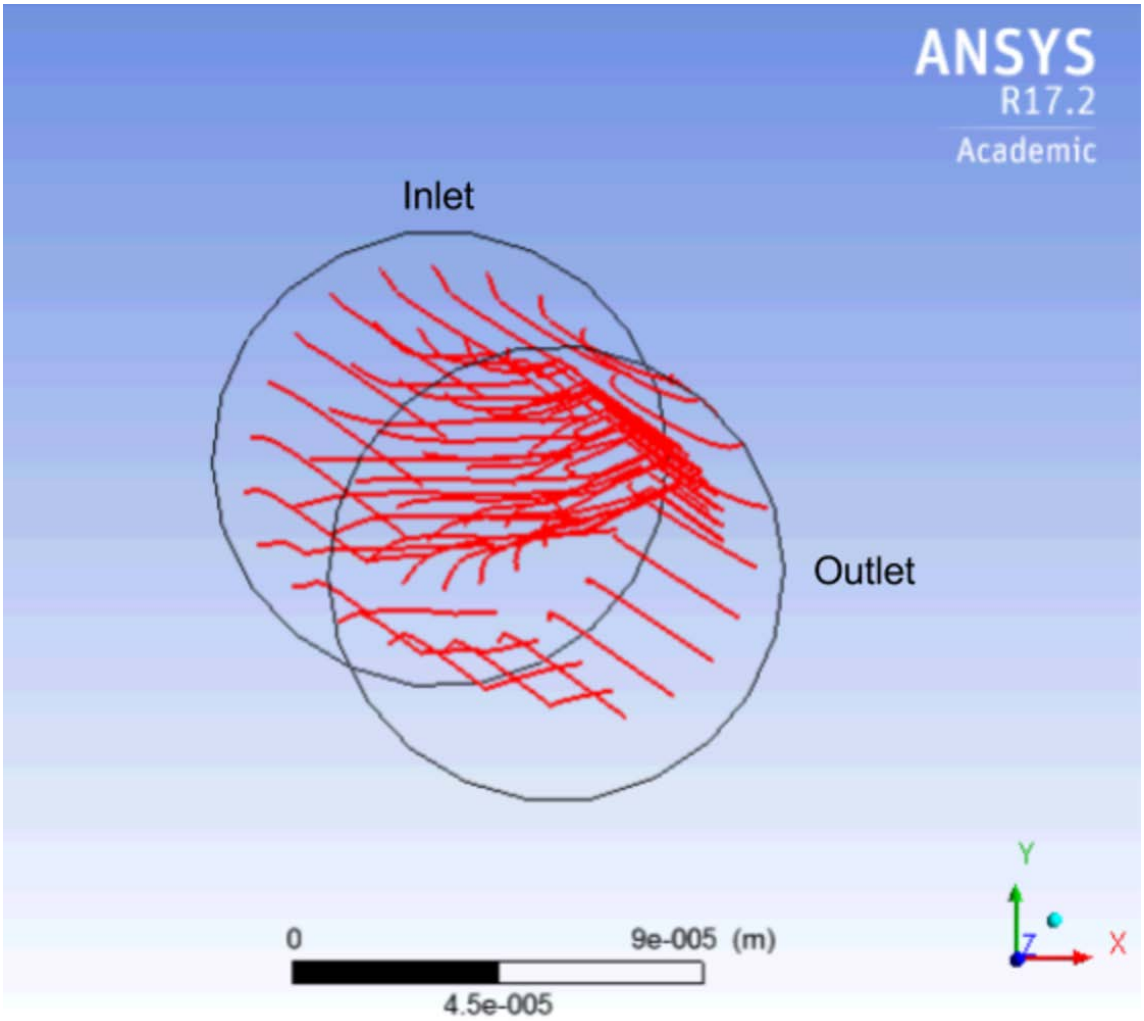

Figure 14: Alternate view of focusing behavior using the al-Amin algorithm.

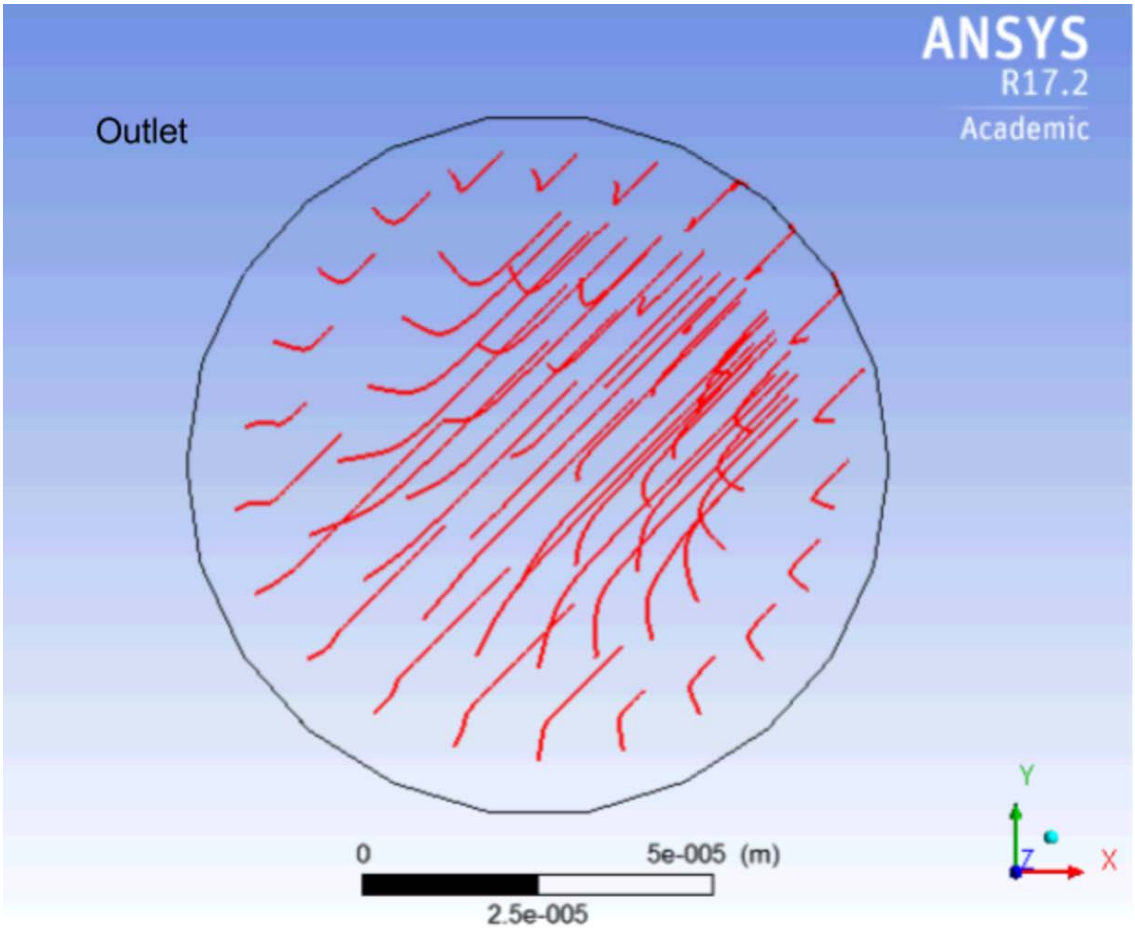

Figure 15: Head-on view of focusing behavior using the al-Amin algorithm at the outlet.

3.9 Refinement of lift modeling

It was determined that the main cause of incorrect focusing behavior was due to an incorrect derivation of the lift coefficient formula used by al-Amin [28]. Experimenting with changing variables in the formula revealed a failure to account for the sign of the force vector. Additionally, comparison of the derivation of the lift coefficient with results from the literature revealed a discrepancy, possibly due to an attempt to model the average lift coefficient given a Reynolds number rather than the lift coefficient as a function of radial position. Based on the results of their theoretical analysis, Ho and Leal proposed a lift coefficient relationship of the form

$$C_L = \beta^2 G_1 + \beta\gamma G_2 ,$$

where β is the dimensionless shear rate, γ is the dimensionless shear gradient, and G_1 and G_2 are functions of the radial position [32]. Liu et al. used this theoretical approach to derive

the coefficient of lift for numerous radial positions in the pipe [32]. A Matlab script was written to determine the lift coefficient as a second-order polynomial function of the relative radial position [Appendix 1]. This resulted in the formula

$$C_L = -43.5484 x_d^2 + 27.5323 x_d ,$$

where x_d is the dimensionless radial position defined as r/R, with an R^2 value of 0.9811. The code was rewritten to include the updated function for the lift coefficient [Appendix 2]. With the adjustment of the lift coefficient relationship, the simulation demonstrates the particles focusing to an annulus equilibrium position of the kind first observed by Segre and Silberberg, as seen in Figures 16-18. Mesh convergence was confirmed by comparing the results at relevance of 100 to relevance of 90 (10% coarser mesh), which demonstrated the same behavior.

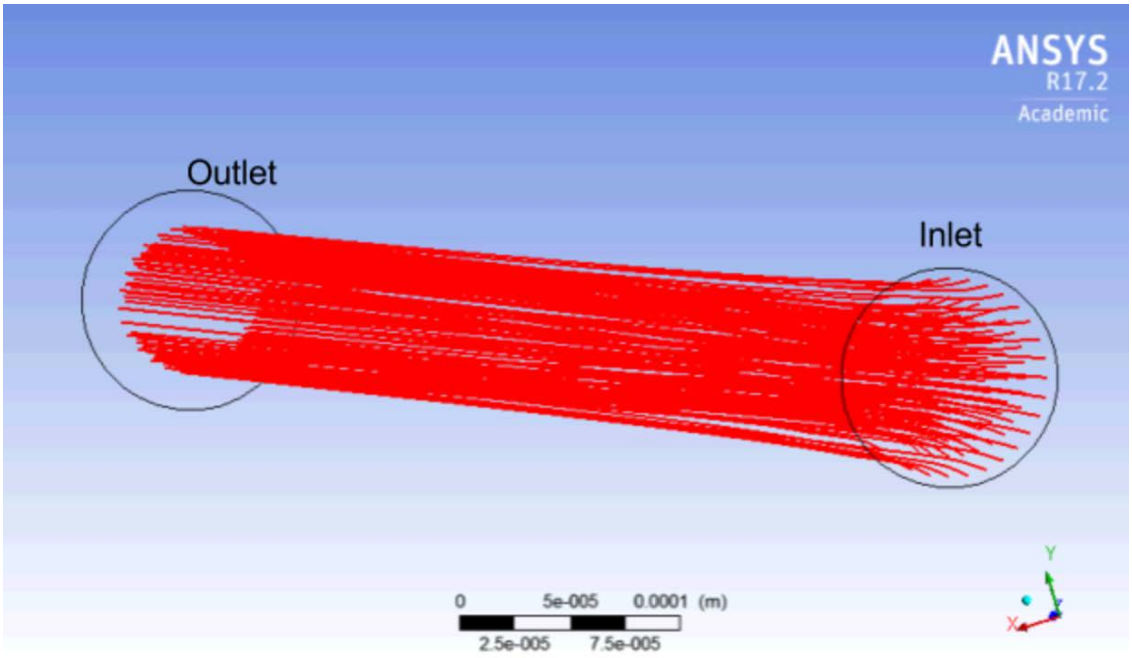

Figure 16: View of the particles focusing to an annulus from the inlet using the refined algorithm.

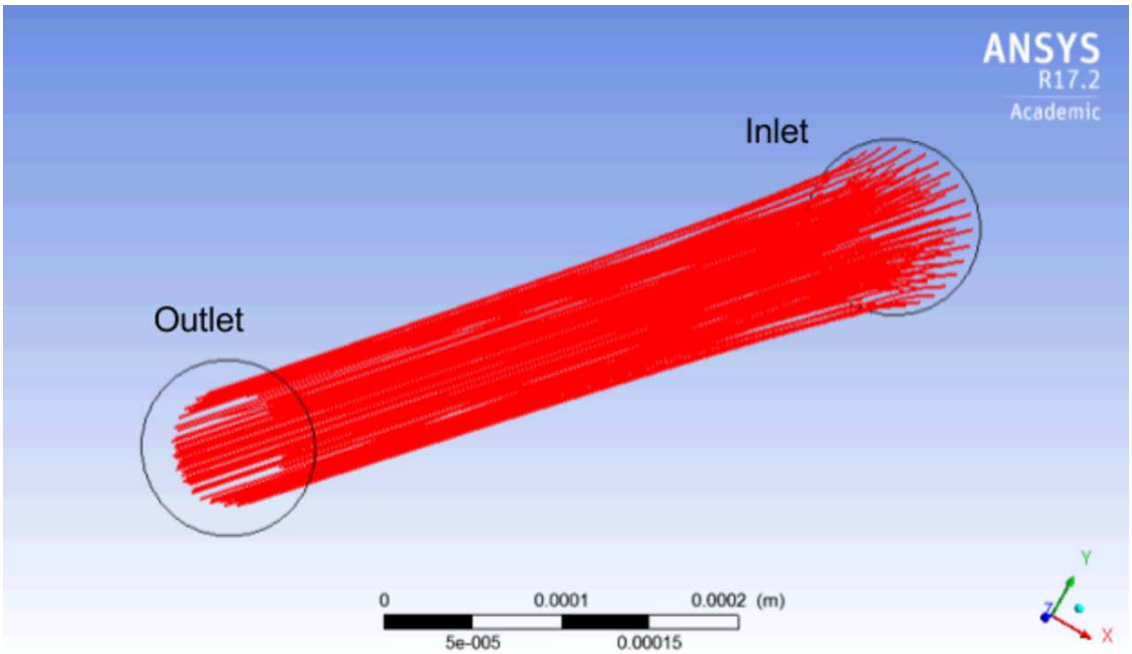

Figure 17: View of particles focusing to an annulus from the outlet using the refined algorithm.

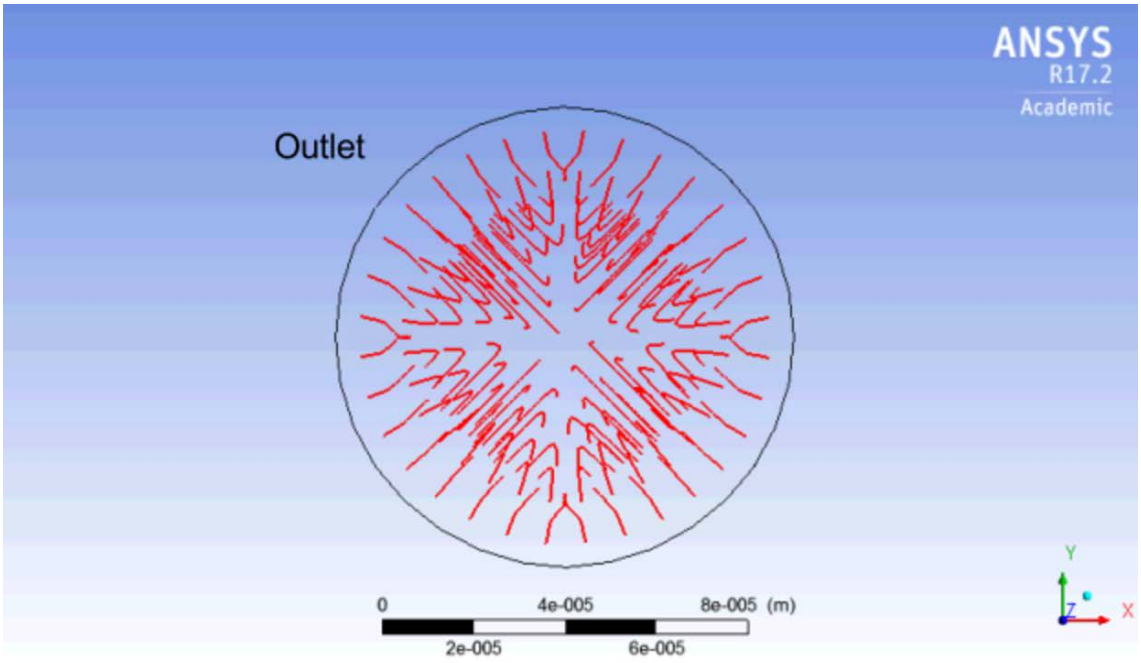

Figure 18: Head-on view of particle focusing behavior at the outlet using the refined algorithm.

This focusing behavior is validated by analyzing the radial positions of the particles at the outlet. The mean value *r/R* for this simulation is 0.612, close to 0.63 from the original Segre Silberberg experiment.

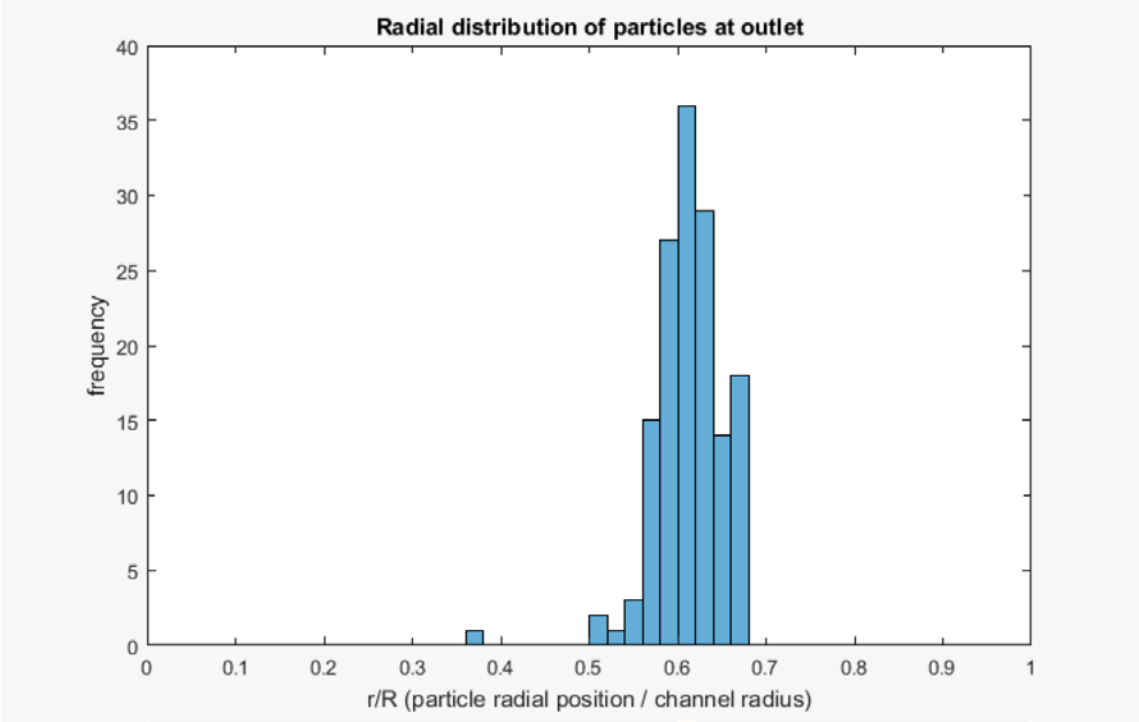

Figure 19: This frequency histogram of particle position at the outlet demonstrates that, in accordance with Segre & Silberberg and others, the particles have migrated to locations centered around ~0.6 of the channel radius.

However, the applicability of this relationship is limited by the fact that Ho and Leal only studied situations where $Re << 1$ and the particle/pipe diameter ratio $\chi << 1$ [32]. Extending this theoretical approach to situations of faster flow ($Re > 1$), Schonberg and Hinch obtained a similar qualitative result but values an order of magnitude smaller than those calculated by Ho and Leal [32]. The accuracy of their work was confirmed by direct numerical simulation undertaken by Liu et al [32]. Again, using the values derived by Liu et al. using this relationship, a Matlab script was written in order to determine a second-order polynomial function for the relationship between lift coefficient and radial position. This resulted in the formula

$$C_L = -3.6919 x_d^2 + 2.2955 x_d ,$$

where x_d is the dimensionless radial position defined as r/R, with an R^2 value of 0.9811. As the average lift magnitude is an order of magnitude smaller than that calculated by Ho and Leal, the focusing behavior does not have time to fully emerge with the same geometry and boundary conditions. As seen in Figure 20, the particles are no longer uniformly distributed, which indicates some migration may be beginning to take place, but no singular equilibrium position has emerged. As predicted by the lift function as well as experimental results [11], the greater magnitude of the wall-induced lift force near the wall means that particles near the wall migrate centripetally more rapidly than the particles near the center migrate centrifugally.

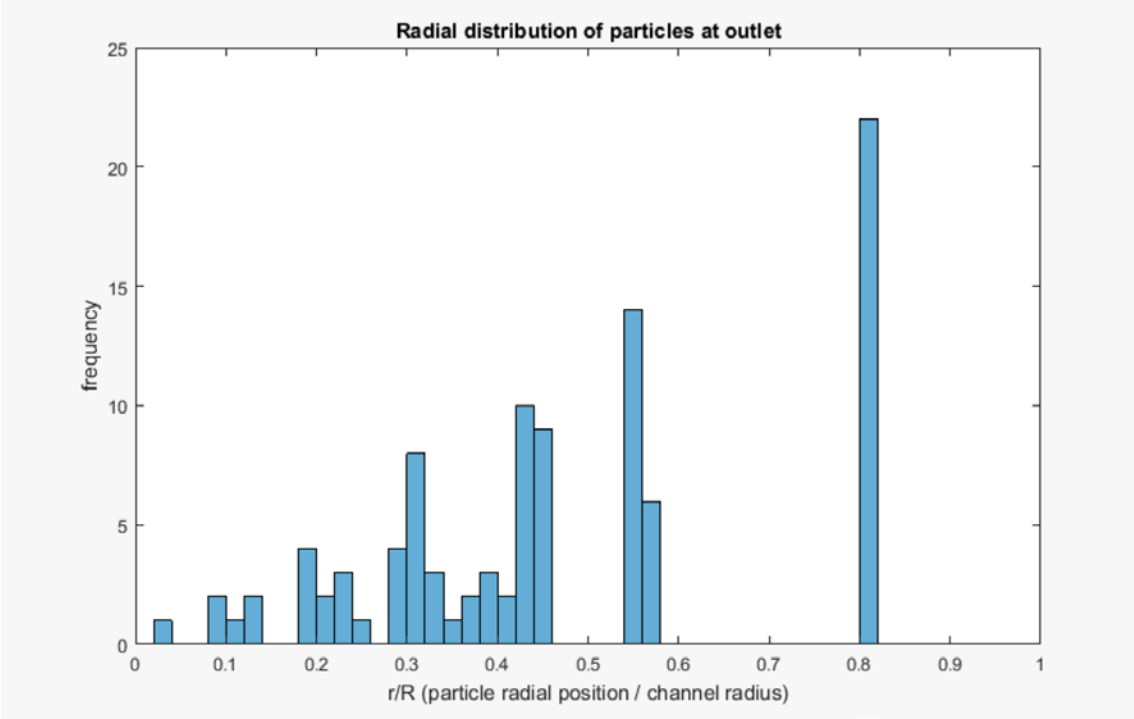

Figure 20: Histogram of particle distribution after 2 mm of pipe length using the Schonberg and Hinch lift formulation.

Increasing the pipe length by an order of magnitude confirmed that the focusing behavior did eventually emerge, albeit at a much further distance than that in the relationship proposed by Ho and Leal. As seen in Figure 21, in a pipe 10x as long as the original model's (L = 20 mm), the particles under the effects of the Schonberg and Hinch lift formulation again approximately focus to the Segre-Silberberg annulus, with a mean value r/R of 0.599.

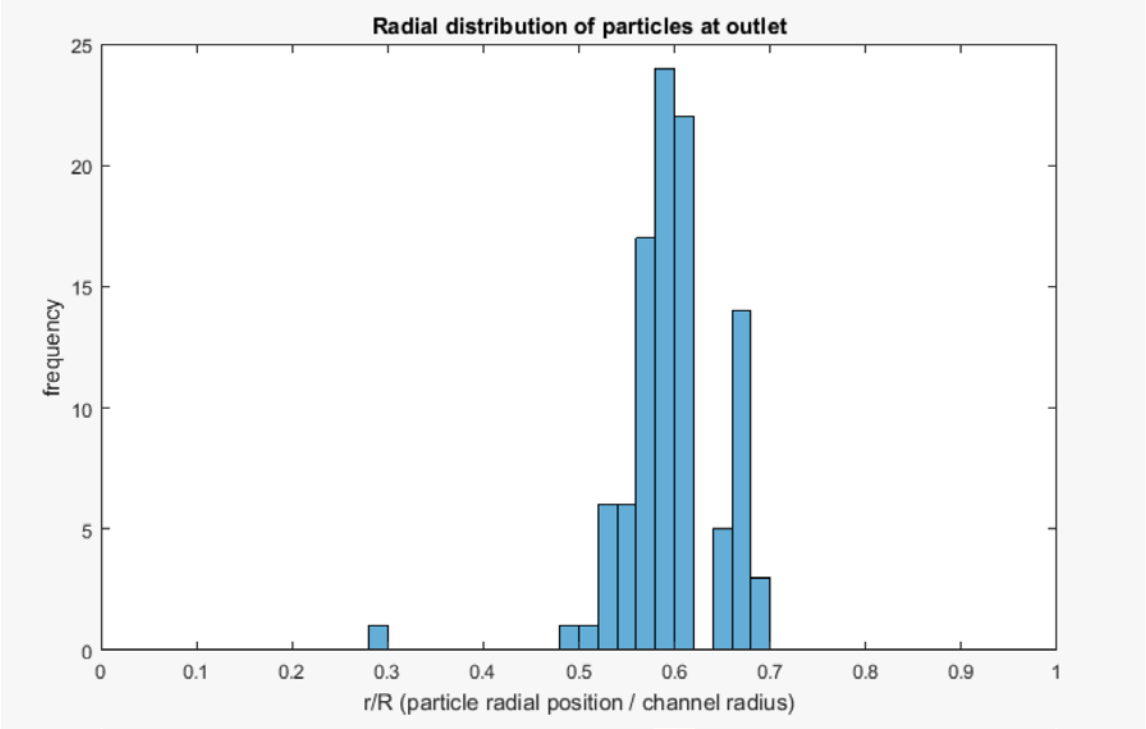

Figure 21: Histogram of particle radial distribution of a pipe 10x as long as the original model's (L = 20 mm).

4 Results

With the successful demonstration of inertial focusing in the situation described above, parameters were varied to observe the change in focusing behavior.

4.1 Variation in particle diameter

Varying the particle size resulted in the behavior below. These simulations were performed at the same Reynolds number of 100 with the Schonberg and Hinch formulation for lift coefficient (valid for $Re > 1$) in the channel length 20 mm.

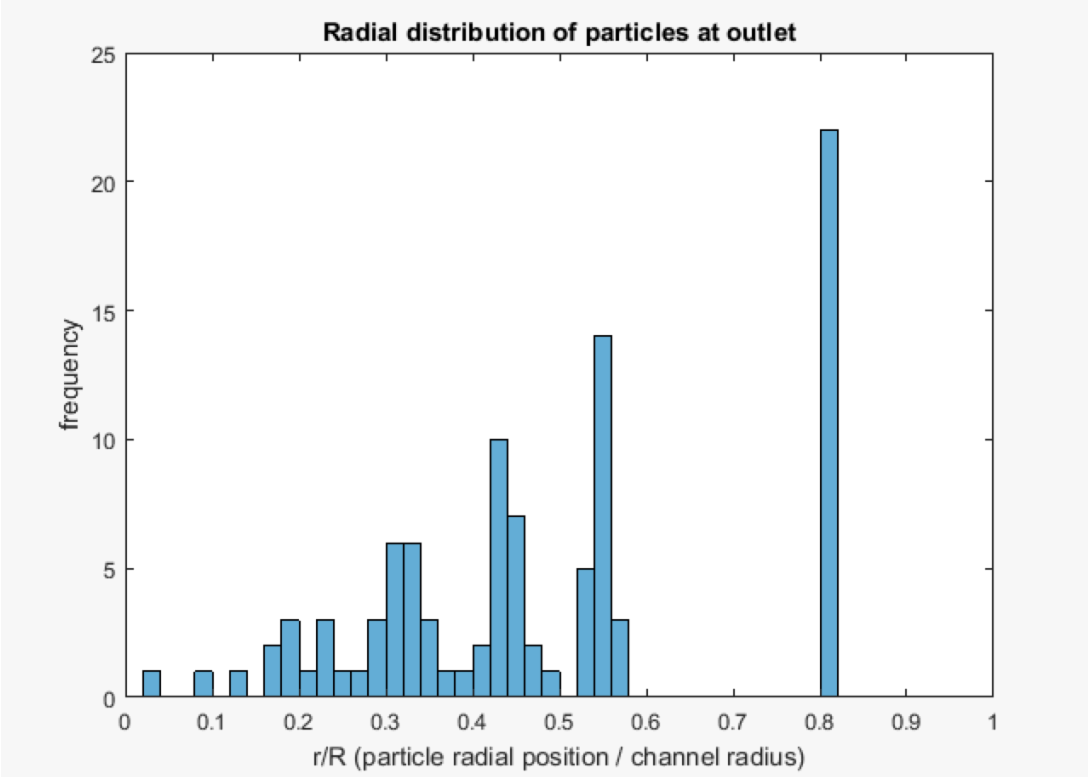

Figure 22: Histogram of radial particle distribution, particle diameter = 1 micron

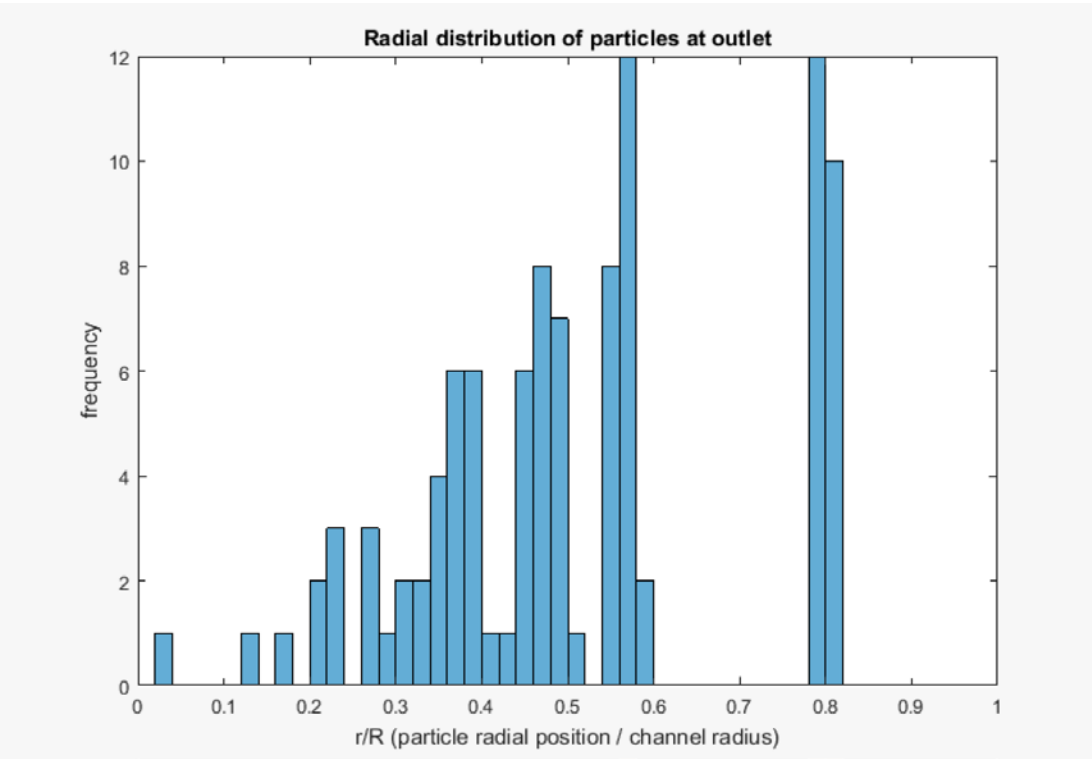

Figure 23: Histogram of radial particle distribution, particle diameter = 2.5 micron

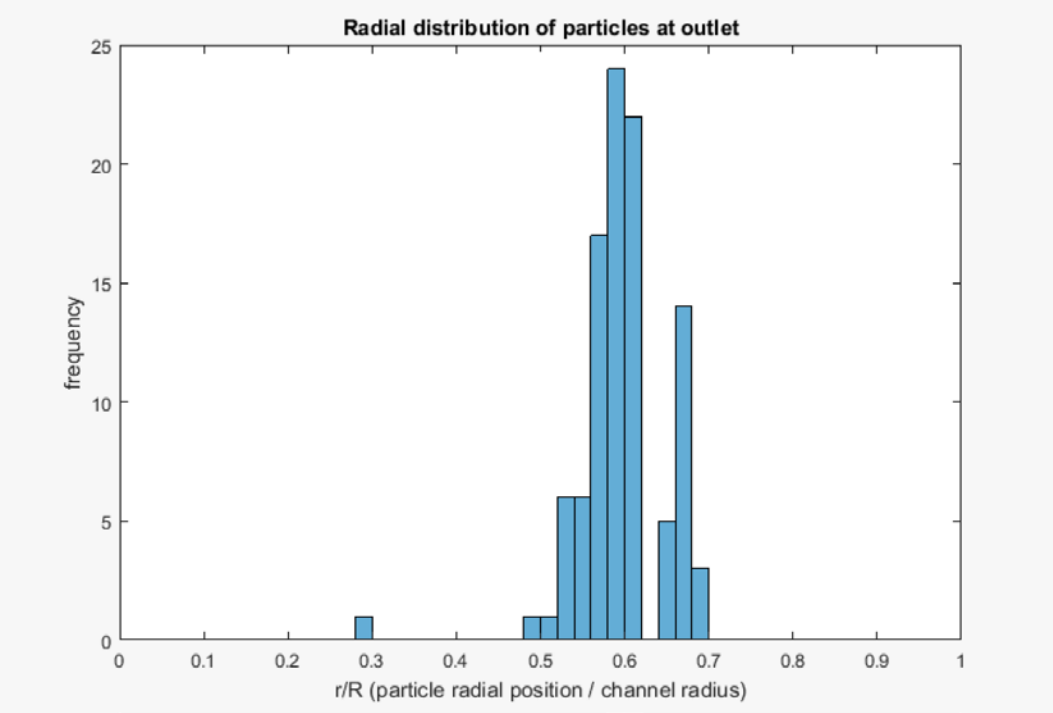

Figure 24: Histogram of radial particle distribution, particle diameter = 5 micron

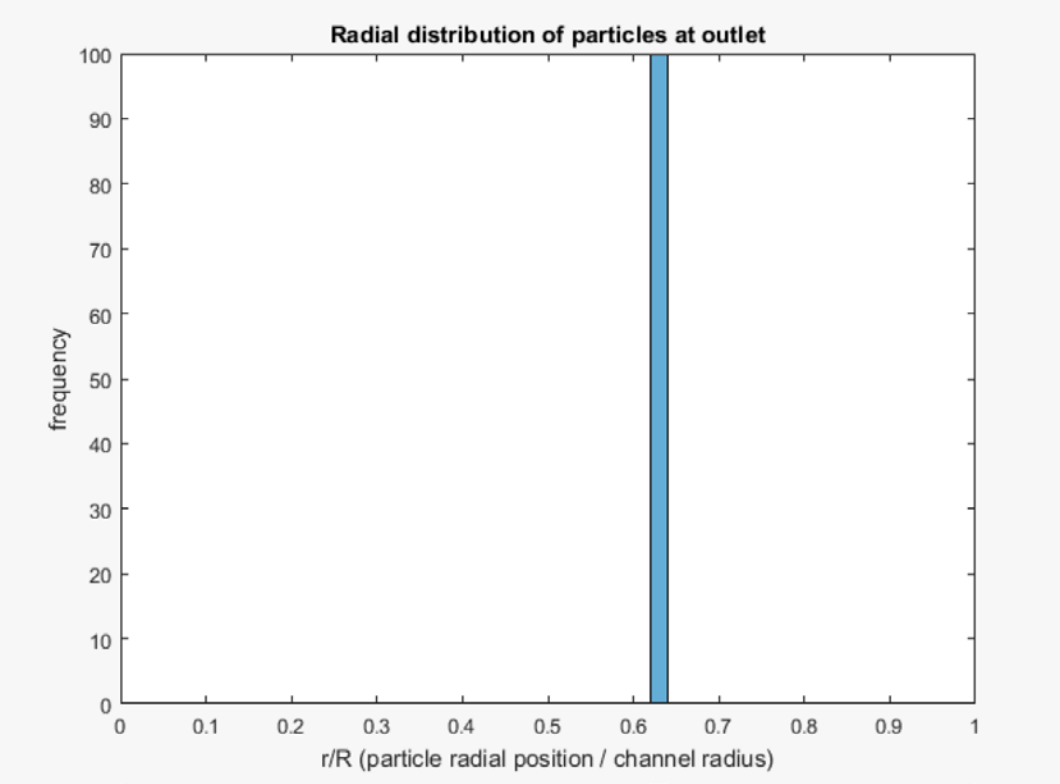

Figure 25: Histogram of radial particle distribution, particle diameter = 10 micron

As predicted from the lift force balance derived above, increasing particle size leads to increasing force. This increases migration velocity and decreases the length of channel required to fully focus the particles. The lift force increases proportionally to a^4, while the mass of constant density increases with the volume of the particle, proportional to a^3. Therefore, as expected, the acceleration experienced by each particle is proportional to its diameter. As seen in the plots above, particles of diameter 1 micron and 2.5 microns do not focus to their equilibrium positions within 20 mm of 100 *Re* flow, although the larger 2.5-micron particle distribution is more clustered than that of the 1 micron particles as demonstrated by the relative frequencies. At 5 microns, all the particles are distributed around the ~0.6 *r/R* annulus, and at 10 microns the distribution has become even tighter, with all the particles falling between 0.62 and 0.64 *r/R*.

4.2 Variation in fluid velocity

Parametric variation was also considered for Reynolds number (i.e. flow velocity), this time keeping constant the original particle diameter of 5 microns and the 20 mm channel length.

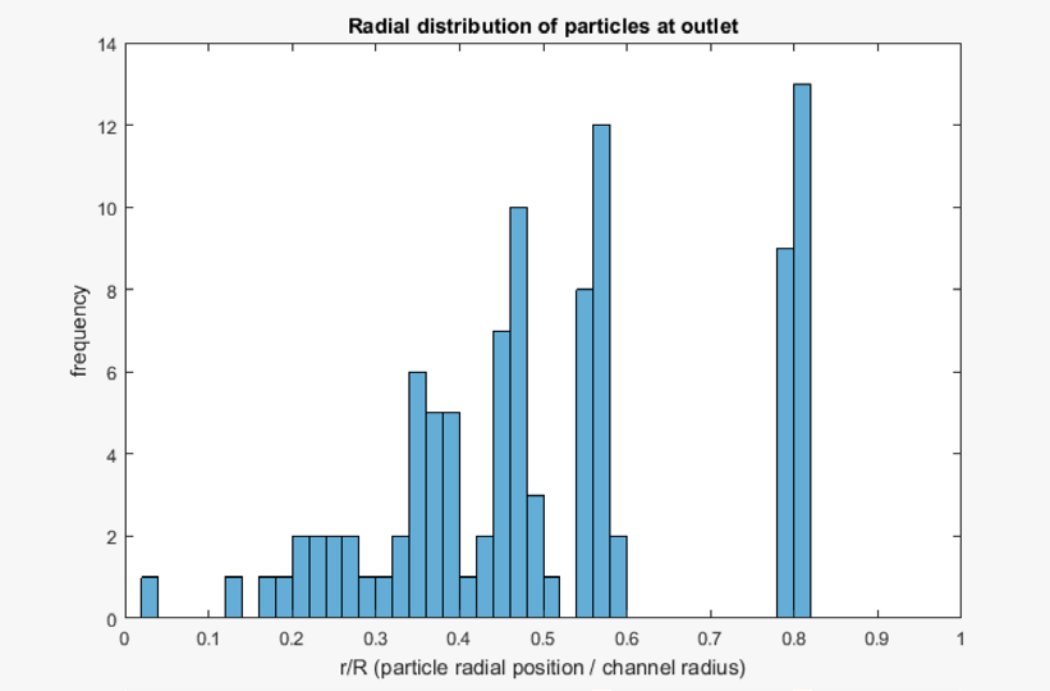

Figure 26: Histogram of radial particle distribution, inlet flow velocity = 0.1 m/s (Re 10)

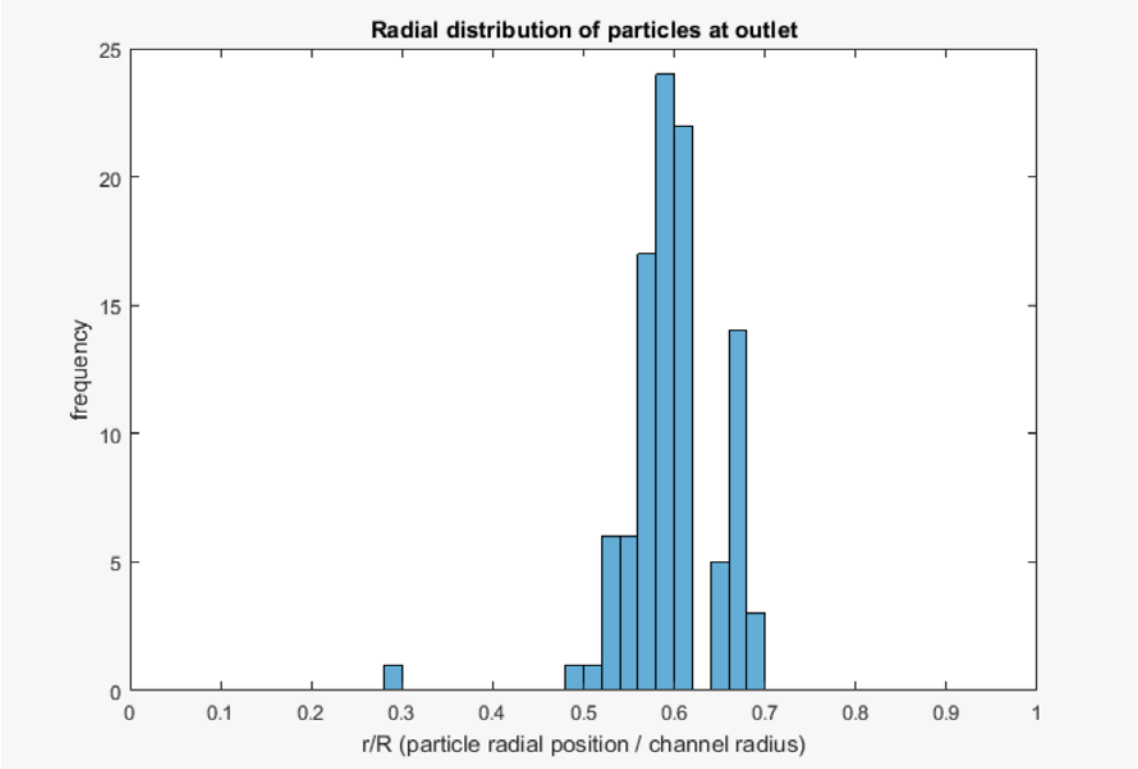

Figure 27: Histogram of radial particle distribution, inlet flow velocity = 1 m/s (Re 100)

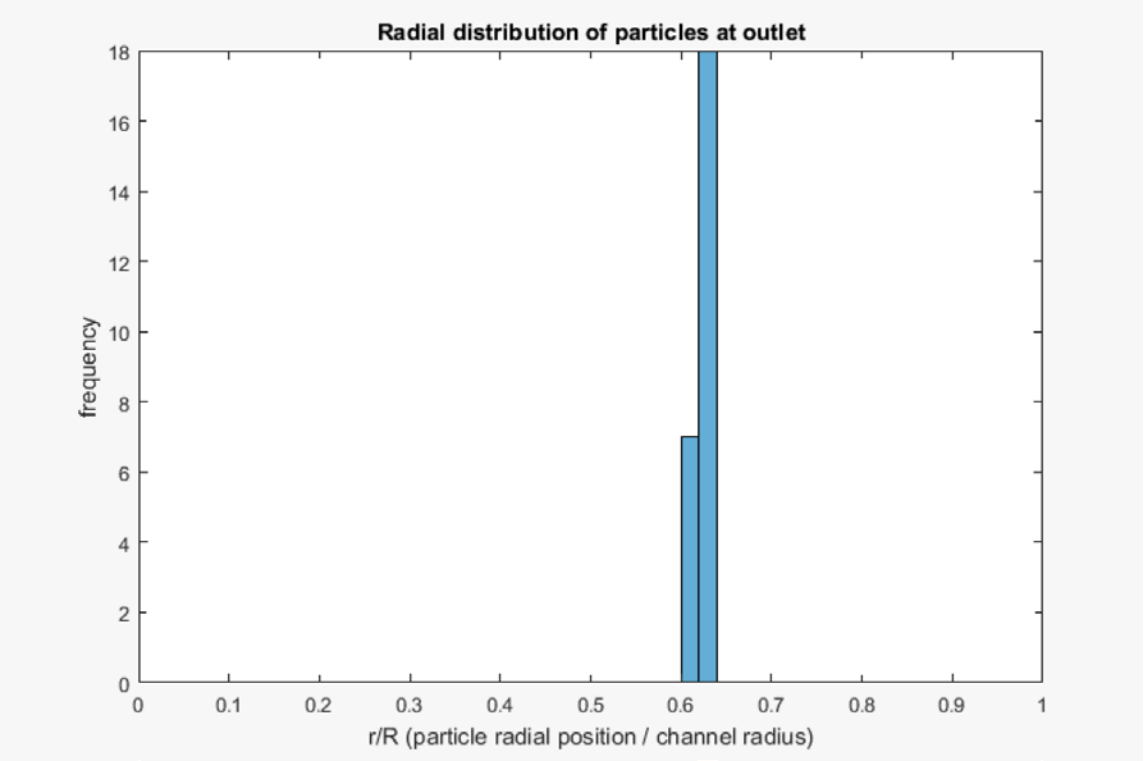

Figure 28: Histogram of radial particle distribution, inlet flow velocity = 2.5 m/s (Re 250)

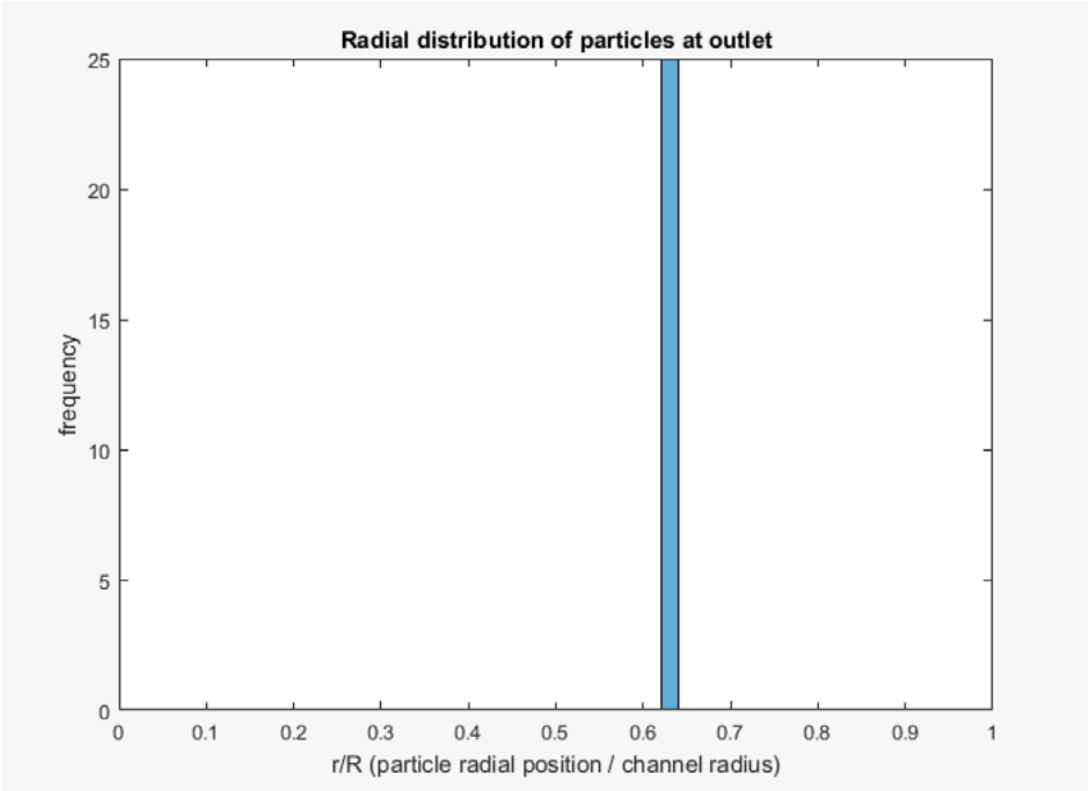

Figure 29: Histogram of radial particle distribution, inlet flow velocity = 5 m/s (500 Re)

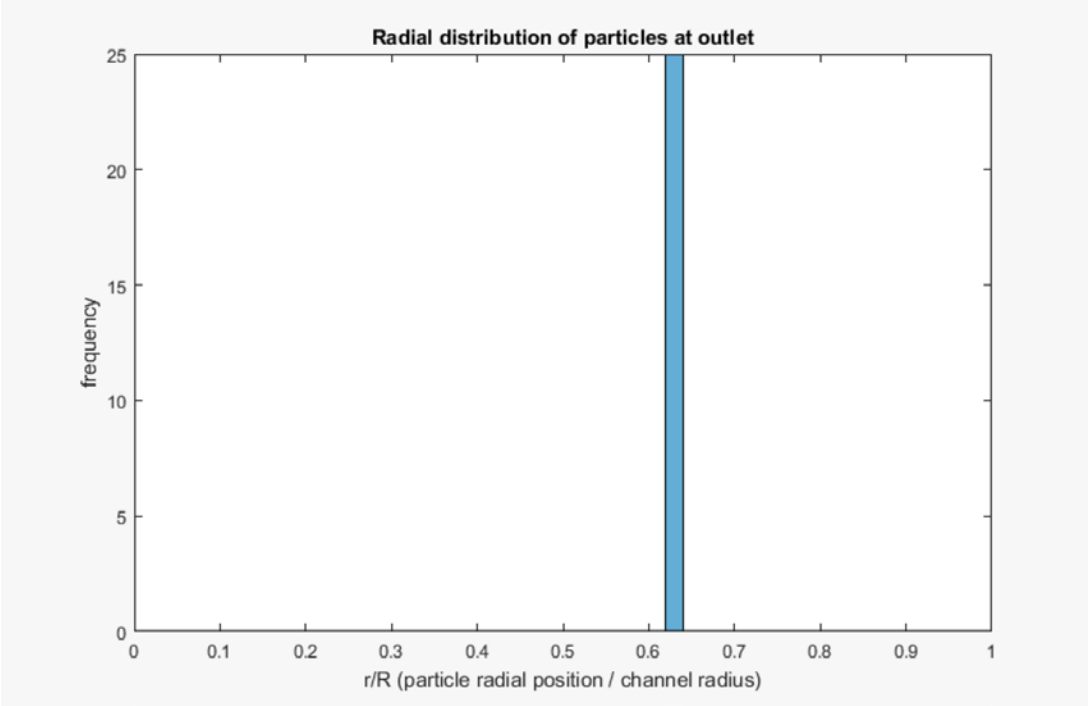

Figure 30: Histogram of radial particle distribution, inlet flow velocity = 7.5 m/s (Re 750)

As predicted from the lift relationship derived earlier, increasing the flow rate increases the average flow velocity and thus the average shear rate. This leads to a larger lift force which means a greater acceleration on each particle and more focusing in the same length of channel. At a *Re* of 10, the particles have just started migrating by the time they reach the outlet, while at a *Re* of 100 they have begun to center around the equilibrium position. As the flow rate continues to increase, the migration speed increases proportionally to U_f^2, leading to even tighter focusing at the outlet. One focusing behavior that was not observed in these results was the emergence of a second inner annulus at Reynolds numbers above 600, first documented experimentally by Matas et al [13]. This is not surprising, given that the derivation of the lift formula only accounts for a force balance at one radial location. Indeed, Matas et al. note that the force balance method alone cannot explain their observations [13]. Possible remedies to this issue are discussed further in conclusions.

In terms of cytometry applications, this agreement of the simulated results with empirical work validates the use of this model for simulating the motion of particles in cytometers as well as predicting the dimensions required for focusing. Using the model would allow a cytometer designer to determine what length of channel is required to achieve full focusing with all the particles clustered on the annulus and travelling the same speed. Being able to predict this constant particle speed would also allow the designer to predict how long a transit of the laser interrogation point would last and thus what trigger time the collection mechanisms should be set for.

5 Conclusions & Future Work

Using the ANSYS Fluent CFD package, a Lagrangian method was developed to simulate the trajectory of microscale particles due to inertial focusing in the laminar regime of straight channels. This method was able to successfully model the focusing behavior of particles in accordance with empirical results in a way less computationally costly than alternative methods such as direct numerical simulation [32]. However, there were a number of limitations to the accuracy of the method which must be addressed in the future before the method can be applied to broader scenarios.

For the limited case of inertial focusing where the net lift force is due to the balance between the wall-induced and shear-induced lift forces, the ultimate trajectory of particles is accurately modeled. Specifically, this refers to situations where neutrally buoyant

spherical particles experience non-negligible laminar flow in straight circular channels. In accordance with multiple experiments, the particles under the influence of a net lift force will migrate to an annulus ~0.6 of the radius of the channel. As observed experimentally, the particles near the walls migrate much faster than those near the center of the channel. Additionally, the net lift force and thus the rapidity with which the particles were observed to migrate to equilibrium positions increased with increasing fluid velocity and increased with increasing particle diameter. This method can thus be used to predict the behavior of particles in microscale channels, which would aid the design of flow cytometers and other microfluidic devices.

However, there are some aspects of the focusing behavior that were not fully accounted for in this model. For instance, the formulation for coefficient of net lift was based on theoretical work by Ho & Leal and Schonberg & Hinch and was modeled as a function of the particle's relative radial position in the channel. Numerical and experimental results indicate that the relationship may be more complicated than this. Increasing the Reynolds number of a flow has been observed to increase the radius of the equilibrium annulus, which indicates that the coefficient of lift is also dependent on the speed of the flow [13]. Direct numerical simulation has suggested that the radius of the equilibrium annulus decreases with increasing particle blockage ratio (ratio of the particle diameter to the channel diameter), which indicates that for a constant diameter channel the coefficient of lift is also dependent on the diameter of the particles [32].

Another behavior not observed with this method was the emergence first observed by Matas et al. of a secondary inner annulus at Reynolds numbers greater than 600 [13]. This behavior cannot be explained just by considering the dependence of the lift coefficient on the Reynolds number, as this would entail a qualitative change in the lift force relationship. Indeed, as yet it is unknown even whether this annulus constitutes a genuinely novel equilibrium position or merely the artifact of slow migration due to a local minimum in the lift force profile [13]. If this behavior is determined to be a genuine equilibrium position, Matas et al. have proposed that it is due to either a failure of the point-particle assumption or an oversimplification of the geometry for modeling purposes, or both [13].

In non-circular (i.e. non-axisymmetric) and non-straight channels, additional force terms would have to be added to the generalized lift force in order to accurately model focusing behavior. In non-circular channels (commonly used in microfluidic channels manufactured with microlithography), this means the addition of a rotational lift term

caused by the asymmetric flow profile. In curved channels, this means the addition of a Dean drag term caused by the recirculation of fluid from the centrifugal pressure gradient. This Dean drag must also be considered in straight channels where obstacles are present [20].

Other changes in the situation settings will also result in the impact of additional forces that will affect the focusing behavior. Non-neutrally buoyant particles require the consideration of buoyant forces. Non-Newtonian fluids experience the impact of gradients in the normal stress about particles due to the non-negligible elasticity of the fluid. Non-spherical particles experience different forces due to their asymmetric nature, and this has been observed empirically in the form of non-standard focusing behavior relative to spherical particles [13]. Interparticle interaction is also neglected in the current model. Cells can be approximated as neutrally buoyant spheres, but further accuracy would require determining more accurate models for the effects of density and geometry. Any future simulation with the goal of modeling situations outside of the limited case of two balanced radial lift forces must therefore also consider the impact of these additional force terms.

Sources

[1] Thermo Fisher Scientific, (2017), *Thermo Fisher Scientific* [Online]. Available: http://www.thermofisher.com/us/en/home.html (Accessed: Feb 12, 2017).

[2] H. Shapiro, *Practical Flow Cytometry,* Hoboken, NJ: Wiley-Liss, 2003.

[3] W. Smith (Staff Systems Engineer, Flow R&D, Thermo Fisher Scientific), *Capstone Full Team Meeting* [Meeting with ME Capstone team, CS Capstone team, N. MacCarty, and S. Le Roux], Corvallis, OR, Oct. 7, 2016.

[4] S.C. Hur, H.T.K. Tse, and D. di Carlo, "Sheathless inertial cell ordering for extreme throughput flow cytometry," *Lab on a Chip,* vol. 10, no. 3, pp. 274-280, 2010.

[5] J. Oakey et al, "Particle focusing in staged inertial microfluidic devices for flow cytometry," *Analytical Chemistry,* vol. 82, no. 9, pp. 3862-3868, 2010.

[6] S. Eyal, S.R. Quake, and G.W. Slater, "Velocity-independent microfluidic flow cytometry," *Electrophoresis,* vol. 23, no. 16, pp. 2653-2657, 2002.

[7] Y. Zhao, B.S. Fujimoto, G.D.M. Jeffries, P.G. Schiro, and D.T. Chiu, "Optical gradient flow focusing," *Optics Express,* vol. 15, no. 10, pp. 6167-6176, 2007.

[8] M. Li et al, "Continuous particle focusing in a waved microchannel using negative dc dielectrophoresis," *Journal of Micromechanics and Microengineering,* vol. 22, no. 9, pp. 95001-95009, 2012.

[9] KAIST NanoBiotech Laboratory, (2012), *Research Highlights* [Online]. Available: http://nanobio.kaist.ac.kr/Res_Hyrdrophoresis.htm (Accessed: Feb 15, 2017).

[10] D. di Carlo, "Inertial microfluidics," *Lab on a Chip,* vol. 9, no. 21, pp. 3038-3046, 2009.

[11] G. Segre and A. Silberberg, "Radial particle displacements in Poiseuille flow of suspensions," *Nature,* vol. 189, no. 4760, p. 209, 1961.

[12] E.J. Lim et al, "Inertio-elastic focusing of bioparticles in microchannels at high throughput," *Nature Communications,* vol. 5, pp. 121-129, 2014.

[13] J-P Matas, J.F. Morris, and E. Guazzelli, "Inertial migration of rigid spherical particles in Poiseuille flow," *Journal of Fluid Mechanics,* vol. 515, pp. 171-195, 2004.

[14] F.P. Bretherton, "The motion of rigid particles in a shear flow at low Reynolds number," *Journal of Fluid Mechanics,* vol. 14, pp. 284–304, 1962.

[15] C. Prohma, M. Gierlak, and H. Stark, "Inertial microfluidics with multi-particle collision dynamics," *The European Physical Journal,* vol. 35, no. 8, pp. 1-10, 2012.

[16] L. Zeng, F. Najjar, S. Balachandar, and P. Fischer, "Forces on a finite-sized particle located close to a wall in a linear shear flow," *Physics of Fluids,* vol. 21, no. 3, 2009.

[17] E.S. Asmolov, "The inertial lift on a spherical particle in a plane Poiseuille flow at large channel Reynolds number," *Journal of Fluid Mechanics,* vol. 381, pp. 63-87, 1999.

[18] J. Zhou and I. Papautsky, "Fundamentals of inertial focusing in microchannels," *Lab on a Chip,* vol. 13, no. 6, pp. 1121-1132, 2013.

[19] D. di Carlo, D. Irimia, R.G. Tompkins, and M. Toner, "Continuous inertial focusing, ordering, and separation of particles in microchannels," *Proceedings of the National Academy of Sciences of the United States of America,* vol. 104, no. 48, pp. 18892-18897, 2007.

[20] J. Zhang, "Fundamentals and applications of inertial microfluidics: a review," *Lab on a Chip,* vol. 16, no. 1, pp. 10-34, 2015.

[21] A.A.S. Bhagat, S.S. Kuntaegowndanahalli, I. Papautsky, "Enhanced particle filtration in straight microchannels using shear-modulated inertial migration," *Physics of Fluids,* vol. 20, no. 10, 2008.

[22] J.M. Martel and M. Toner, "Inertial focusing dynamics in spiral microchannels," *Physics of Fluids,* vol. 24, no. 3, 2012.

[23] J.F. Wendt, *Computational Fluid Dynamics: An Introduction,* Sint-Genesius-Rode, Belgium: von Karman Institute for Fluid Dynamics, 1996.

[24] B.H. Yang et al, "Migration of a sphere in tube flow," *Journal of Fluid Mechanics,* vol. 540, pp. 109-131, 2005.

[25] J. Feng, H.H. Hu, and D.D. Joseph, "Direct simulation of initial value problems for the motion of solid bodies in a Newtonian fluid. Part 2. Couette and Poiseuille flows," *Journal of Fluid Mechanics,* vol. 277, pp. 271-301, 1994.

[26] A.A.S. Bhagat, S.S. Kuntaegowdanahalli, and I. Papautsky, "Continuous particle separation in spiral microchannels using dean flows and differential migration," *Lab on a Chip,* vol. 8, no. 11, pp. 1906-1914, 2008.

[27] G. Guan et al, "Spiral microchannel with rectangular and trapezoidal cross-sections for size based particle separation," *Scientific Reports,* vol. 3, 2013.

[28] A. al-Amin, "High throughput particle separation using differential Fermat spiral microchannel with variable channel width," M.S. thesis, Dept. Mech. Eng., University of Akron, Akron, OH, 2015.

[29] *ANSYS Fluent User's Manual,* Ansys Inc., Canonsburg, PA, 2016.

[30] J.P. Holman, *Heat Transfer,* New York, NY: McGraw-Hill, 2002.

[31] T.L. Bergman and F.P. Incropera, *Fundamentals of Heat and Mass Transfer,* Hoboken, NJ: Wiley, 2011.

[32] C. Liu, C. Xue, J. Sun, and G. Hu, "A generalized formula for inertial lift on a sphere in microchannels," *Lab on a Chip,* vol. 16, no. 5, pp. 884-892, 2016.

[33] J. Schonberg and E.J. Hinch, "Inertial migration of a sphere in Poiseuille flow," *Journal of Fluid Mechanics,* vol. 203, p. 517-524, 1989.

Appendix 1

```
% Matlab code for calculating lift coefficient function (Ho and Leal)

clear all
clc
clf
close all

% define column vectors of radial position
% and lift coefficient
x = [0,.2,.4,.6,.8];
y = [0,4,4.5,0,-5.5];
xp = x.';
yp = y.';

% solve system of equations constrained at origin
a123 = [xp.^2,xp]\yp

% plot polynomial for comparison
x1 = linspace(0,1);
f1 = polyval([a123; 0],x1);

figure
plot(x,y,'o')
hold on
plot(x1,f1)

% calculate R squared
yresid = y - polyval([a123; 0],x);
SSresid = sum(yresid.^2);
SStotal = (length(y)-1) * var(y);
rsq = 1 - SSresid/SStotal
```

Appendix 2

```
/* UDF for computing the lateral displacement of particle suspended in fluid flow*/

#include "udf.h"
#include "mem.h" /* cell indexing header */
#include "dpm.h" /* particle properties even though declared in the macro arguments */
/* #include "metric.h" */
/*#include <math.h> */

DEFINE_DPM_BODY_FORCE(asmolov_lift_7,p,i)
{
        /* declaration of variables */
        double w, Dh, Ufx, Ufy, Ufz, Gx, Gy, Gz, rho, a, Fx, Fy, Fz, FL, c_height, c_length,
c_volume, side,
height, width, f_height_total, Renx, Reny, Renz, crDh, mu, aUfx, aUfy, aUfz, Clx, Cly, Clz, r, xd;

        cell_t c = P_CELL(p); /* the cell initialization in which the particle is present*/
        Thread *t = P_CELL_THREAD(p); /* thread initialization */
        c_volume = C_VOLUME(c,t);

        c_height = 0.00001; /* these values varies depending upon mesh cell sizes*/
        c_length = 0.00015; /* these values varies depending upon mesh cell sizes*/
        side = c_volume/(c_height*c_length); /* calculating the width of mesh cell for Dh
calculations*/
height = 0.00005;
        width = 12*side;
        Dh = 0.0001;
        crDh = pow(c_volume, (1./3.));
        mu = 0.001003;
        rho = C_R(c,t);
        Ufx = C_U(c,t);
        Ufy = C_V(c,t);
```

```
Ufz = C_W(c,t);
aUfx = fabs(Ufx);
aUfy = fabs(Ufy);
aUfz = fabs(Ufz);

/* local Reynolds number calculation*/
Renx = (rho*aUfx*crDh)/mu;
Reny = (rho*aUfy*crDh)/mu;
Renz = (rho*aUfz*crDh)/mu;

/*lift force calculation*/
r = sqrt((pow(P_POS(p)[0],2)) + (pow(P_POS(p)[1],2)));
xd = r/(Dh/2);
Clx = (-43.5484*(pow(xd,2))) + (27.5323*xd);
Cly = Clx;
Clz = Clx;
Gx = (Ufx)/Dh;
Gy = (Ufy)/Dh;
Gz = (Ufz)/Dh;
a = P_DIAM(p); /* particle diameter */
Fx = Clx*rho*pow(Gx,2)*pow(a,4);
Fy = Cly*rho*pow(Gy,2)*pow(a,4);
Fz = Clz*rho*pow(Gz,2)*pow(a,4);

/*calculate sign*/
if (i==0)
{
        if (P_POS(p)[0]>0)
        {
        FL = (Fy+Fz); /* resultant of shear rate tensor*/
        }
        else
        {
```

```
            FL = -(Fy+Fz); /* resultant of shear rate tensor*/
            }
        }
        else if (i==1)
        {
            if (P_POS(p)[1]>0)
            {
                FL = (Fx+Fz); /* resultant of shear rate tensor*/
            }
            else
            {
                FL = -(Fx+Fz); /* resultant of shear rate tensor*/
            }
        }
        else if (i==2)
        {
        FL = Fx+Fy;
        }
        else
        {
        FL = 0;
        }

        return (FL/P_MASS(p));

}
```

Appendix 3

```
% Matlab code for calculating lift coefficient function (Schonberg and Hinch)

clear all
clc
clf
close all

% define column vectors of radial position
% and lift coefficient
x = [0,.1,.2,.3,.4,.5,.6,.63,.7,.8];
y = [0,.14,.24,.34,.36,.24,.09,0,-0.2,-0.57];
xp = x.';
yp = y.';

% solve system of equations constrained at origin
a123 = [xp.^2,xp]\yp

% plot polynomial for comparison
x1 = linspace(0,1);
f1 = polyval([a123; 0],x1);

figure
plot(x,y,'o')
hold on
plot(x1,f1)

% calculate R squared
yresid = y - polyval([a123; 0],x);
SSresid = sum(yresid.^2);
SStotal = (length(y)-1) * var(y);
rsq = 1 - SSresid/SStotal
```